Climate impacts of parameterized Nordic Sea overflows

Gokhan Danabasoglu,[1] William G. Large,[1] and Bruce P. Briegleb[1]

Received 8 March 2010; revised 24 June 2010; accepted 22 July 2010; published 6 November 2010.

[1] A new overflow parameterization (OFP) of density-driven flows through ocean ridges via narrow, unresolved channels has been developed and implemented in the ocean component of the Community Climate System Model version 4. It represents exchanges from the Nordic Seas and the Antarctic shelves, associated entrainment, and subsequent injection of overflow product waters into the abyssal basins. We investigate the effects of the parameterized Denmark Strait (DS) and Faroe Bank Channel (FBC) overflows on the ocean circulation, showing their impacts on the Atlantic Meridional Overturning Circulation and the North Atlantic climate. The OFP is based on the Marginal Sea Boundary Condition scheme of Price and Yang (1998), but there are significant differences that are described in detail. Two uncoupled (ocean-only) and two fully coupled simulations are analyzed. Each pair consists of one case with the OFP and a control case without this parameterization. In both uncoupled and coupled experiments, the parameterized DS and FBC source volume transports are within the range of observed estimates. The entrainment volume transports remain lower than observational estimates, leading to lower than observed product volume transports. Due to low entrainment, the product and source water properties are too similar. The DS and FBC overflow temperature and salinity properties are in better agreement with observations in the uncoupled case than in the coupled simulation, likely reflecting surface flux differences. The most significant impact of the OFP is the improved North Atlantic Deep Water penetration depth, leading to a much better comparison with the observational data and significantly reducing the chronic, shallow penetration depth bias in level coordinate models. This improvement is due to the deeper penetration of the southward flowing Deep Western Boundary Current. In comparison with control experiments without the OFP, the abyssal ventilation rates increase in the North Atlantic. In the uncoupled simulation with the OFP, the warm bias of the control simulation in the deep North Atlantic is substantially reduced along with salinity bias reductions in the northern North Atlantic. There are similar but more modest bias reductions in the deep temperature and salinity distributions especially in the northern North Atlantic in the coupled OFP case. In coupled simulations, there are noticeable impacts of the OFP on climate. The sea surface temperatures (SSTs) are warmer by more than 5°C off the North American coast and by more than 1°C in the Nordic Sea with the OFP. The surface heat fluxes mostly act to diminish these SST changes. There are related changes in the sea level pressure, leading to about 15% weaker westerly wind stress in the northern North Atlantic. In response to the warmer Nordic Sea SSTs, there are reductions in the sea ice extent, improving comparisons with observations. Although the OFP cases improve many aspects of the simulations compared to observations, some significant biases remain, more in coupled than in uncoupled simulations.

Citation: Danabasoglu, G., W. G. Large, and B. P. Briegleb (2010), Climate impacts of parameterized Nordic Sea overflows, *J. Geophys. Res.*, *115*, C11005, doi:10.1029/2010JC006243.

1. Introduction

[2] The Atlantic Meridional Overturning Circulation (AMOC) with its associated heat and salt transports significantly influences the climate of the North Atlantic and surrounding areas. Many coupled climate modeling studies [e.g., *Delworth et al.*, 1993] suggest that changes in the AMOC affect the Sea Surface Temperature (SST) variability. Through atmospheric interactions, these SST changes can impact even the global climate on interannual and (multi) decadal time scales [see *Hurrell et al.*, 2006, and references therein]. In addition, major changes in the AMOC have been implicated to explain some past abrupt climate change events [e.g., *Broecker*, 2003]. Motivated by its prominent role in

[1]National Center for Atmospheric Research, Boulder, Colorado, USA.

0148-0227/10/2010JC006243

the Earth's climate system and potential predictability of its variations on decadal and longer time scales [*Griffies and Bryan*, 1997], the AMOC and its behavior under various climate scenarios have been the subject of many recent studies [e.g., *Meehl et al.*, 2006; *Nakashiki et al.*, 2006; *Danabasoglu*, 2008]. The overflow waters from the Nordic Sea through the Denmark Strait (DS) and the Faroe Bank Channel (FBC) combine with the Labrador Sea deep convection to supply the lower branch of the AMOC, known as the North Atlantic Deep Water (NADW). These two gravity currents are flows of dense waters formed in the Nordic Sea. In general, such overflows include three processes: water exchange dynamics as they flow through narrow straits or channels, entrainment of ambient waters as they descend down the continental slopes, and finally intrusion at the depth where they are either neutrally buoyant or they become a bottom density current.

[3] The small-scale nature of these overflow processes with horizontal and vertical length scales as small as 1 km and 10 m, respectively, requires finer horizontal and vertical resolutions than usual for their proper explicit representations in Ocean General Circulation Models (OGCMs). Most of the present-day OGCMs used in coupled climate studies employ horizontal resolutions of about 1°, while their vertical resolutions are about 50–200 m in the mid-depth and abyssal oceans. Therefore, the overflow processes remain subgrid scale in these models. Indeed, *Riemenschneider and Legg* [2007] demonstrate that the FBC overflow structure and the entrainment magnitude become comparable to observations only in their highest-resolution simulation with a 2 km horizontal and 25 m vertical resolution. Similarly, *Chang et al.* [2009] report reasonable DS and FBC overflow properties only with their finest 1/12° horizontal resolution model version.

[4] The entrainment by the overflow waters can strongly depend on a model's vertical coordinate system [*Griffies et al.*, 2000]. In particular, the flows over staircase topography in a level coordinate model tends to have excessive convective entrainment, resulting in deep waters that are too light and that remain too shallow [*Roberts et al.*, 1996; *Winton et al.*, 1998]. Even if a model with a cold Nordic Sea produces the densest possible source waters, the properties of the product water will be quite different than observed due to poorly represented mixing. This represents a long-standing, shallow penetration depth bias of the NADW in level coordinate models compared to observations. The recent observations of the AMOC at 26.5°N (RAPID) [*Cunningham et al.*, 2007] give estimates of the 4 year mean (April 2004 to April 2008) NADW depth, denoted here D_{AMOC}, as about 4350 m. In contrast, in most level coordinate models, D_{AMOC} remains much shallower, e.g., 3000–3400 m in the work of *Bryan et al.* [2006]. One simple approach to remedy this bias has been to artificially modify a model's bottom topography to widen narrow pathways and to deepen downstream of these channels to reduce excessive entrainment in overflow regions. In addition to its ad hoc nature, *Roberts and Wood* [1997] show uncomfortably large sensitivities of the model solutions to seemingly small bottom topography changes in the DS and Iceland-Scotland ridge in a level coordinate ocean model. Another approach is to use very high-resolution nested grids in overflow regions. Despite its potential, this path presents technical challenges primarily involving two-way grid interactions, and hence has not been pursued. We also note that use of shaved/partial bottom cells does not appear to lead to improvements in steep-sloped regions such as the overflow areas [see *Griffies et al.*, 2000].

[5] An attractive alternative to the above approaches is to parameterize the overflows to include their effects in OGCMs of any resolution. Given, for example, the intimate relationship between the DS and FBC overflows and the AMOC and the AMOC's prominent role in affecting the Earth's climate, such overflow parameterizations should be physically based to produce accurate and credible simulations and predictions of the AMOC behavior and its variability. As reviewed by *Tang and Roberts* [2005], several bottom boundary layer parameterizations have been developed to represent the dense water overflows in OGCMs [e.g., *Beckmann and Doescher*, 1997; *Campin and Goosse*, 1999; *Killworth and Edwards*, 1999]. Some of these parameterizations [e.g., *Beckmann and Doescher*, 1997] have been used in various ocean models with some mixed results [e.g., *Doney and Hecht*, 2002; *Griffies et al.*, 2005; *Tang and Roberts*, 2005].

[6] Another set of parameterizations for overflows is based on *streamtube* approaches [*Smith*, 1975; *Killworth*, 1977; *Price and Baringer*, 1994; *Emms*, 1997]. In particular, *Price and Yang* [1998; hereafter PY98] construct an overflow parameterization as a Marginal Sea Boundary Condition (MSBC) for an OGCM. This scheme uses the *Whitehead et al.* [1974] model for maximal geostrophic source flow through a strait. Then, entrainment is described by an end-point model of entraining, rotating density current following *Price and Baringer* [1994]. The mixed product water is then passed to the ocean model for injection at a suitable depth. PY98 along with some other recent overflow parameterizations [e.g., *Kosters et al.*, 2005; *Born et al.*, 2009] assumes that both the DS and FBC overflows are hydraulically controlled. This has only recently been confirmed to be a rather good assumption for both overflows [*Kosters*, 2004; *Girton et al.*, 2006; *Enmar et al.*, 2009]. We also note that the parameterization of entrainment due to shear-driven mixing remains an active research area with parameterizations based on a critical Froude number as in the work of *Price and Baringer* [1994] [e.g., *Hallberg*, 2000; *Xu et al.*, 2006; *Jackson et al.*, 2008], schemes that also include subcritical Froude number entrainment [e.g., *Cenedese and Adduce*, 2010], and others, for example, that are based on second-order turbulent closures [e.g., *Ilicak et al.*, 2008a, 2008b, 2009].

[7] Recently, *Wu et al.* [2007] have used a Parameterized Mediterranean Overflow (PMO) based on this MSBC scheme to successfully incorporate the effects of the Mediterranean overflow through the Strait of Gibraltar. However, the PMO is restricted to cases where the overflow is balanced by inflow directly above it, as is the case at Gibraltar. In the present study, we remove this restriction, and develop a new overflow parameterization (OFP) for flows through deep ridges via channels (e.g., DS and FBC) and continental shelf (e.g., Weddell and Ross Sea) overflows. Although the OFP is based on the PY98 MSBC scheme, there are substantial differences between the two. First, in the OFP, the input fields for the exchange and entrainment formulas evolve prognostically. Secondly, the marginal seas providing the

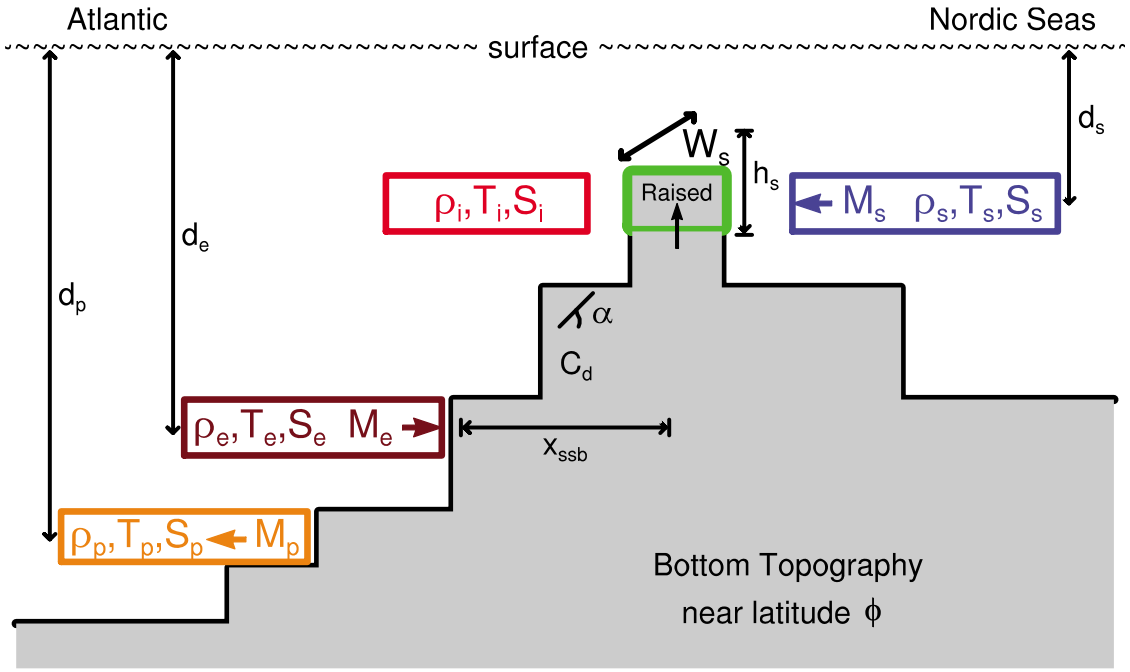

Figure 1. A schematic of the Nordic Sea overflows. T, S, ρ, and M represent potential temperature, salinity, density, and volume transport, respectively. The subscripts s, i, e, and p refer to properties of the overflow source water at the sill depth, the interior water at the sill depth, the entrainment water, and the product water, respectively. The thick, short arrows indicate flow directions. The sill depth lies within the green box of raised bottom topography. The other boxes (except the orange product box) represent the regions whose T and S are used to compute the necessary densities. All parameters shown in black are constants specified for a particular overflow (Table 1). See section 2 for further details.

overflow source waters (e.g., the Nordic Sea) are part of the prognostic model domain rather than just some marginal sea boundary conditions as in the MSBC, and the inflow into these marginal seas is accomplished by the prognostic flow in contrast with a parameterized inflow in the MSBC. Finally, treatment of the baroclinic and barotropic momentum and continuity equations is entirely new.

[8] In our implementation here, we focus on the Nordic Sea overflows for two reasons: (1) there are considerably more observational estimates of the DS and FBC overflow properties than for the Ross and Weddell Sea overflows, thus making an assessment of the OFP in comparison with the observations more meaningful, and (2) both the DS and FBC directly affect the AMOC with potentially important impacts on climate. Therefore, this study concerns examining the impacts of the parameterized DS and FBC overflows on the ocean circulation and climate, focusing on the North Atlantic. We pay particular attention to the effects of these parameterized overflows on D_{AMOC}. In the present work, FBC parameterization includes only the overflow branch between the Faroe Bank and Faroe Islands, carrying the largest fraction of the total estimated overflow transport across the Scotland-Iceland Ridge. The paper is organized as follows. Section 2 and Appendix A present the OFP and a summary of its implementation in the Community Climate System Model version 4 (CCSM4). An assessment of the OFP in comparison with available observations is given in Appendix B and summarized in section 3. The numerical model and experiments are described in section 4. The model results from both ocean-only and fully coupled climate simulations are presented in section 5. We use the ocean-only cases for verification of the OFP, while the coupled cases are used primarily to document climate impacts. Finally, a summary and discussions are given in section 6.

2. Overflow Parameterization

[9] In this section, we present a brief summary of the OFP, noting differences with the PMO. Further details of the scheme are given in Appendix A, and a complete description can be found in *Briegleb et al.* [2010; available at http://www.cgd.ucar.edu/oce/about/staff/gokhan/]. Throughout the manuscript, the subscripts i, s, e, and p are used to denote interior, source, entrainment, and product water properties, respectively. Figure 1 is a schematic representation of the key parameters of a parameterized overflow: the latitude, ϕ, the sill depth, d_s, the width of the channel at the sill, W_s, the thickness of the overflow at the sill, h_s, the depth of the entrainment at the shelf break, d_e, the maximum bottom slope near the shelf break, α, the distance from the sill to the shelf break, x_{ssb}, and the bottom drag coefficient, C_d. Values for all these parameters as specified for both the DS and FBC are given in Table 1.

[10] In Figure 1, the vertical cross section of the bottom topography is shown as it might be represented in a level coordinate model. With the usual prognostic, rather than parameterized, overflow, the model level corresponding to the sill depth (the green grid cell in Figure 1) is above the

Table 1. Specified Parameters (Constants in the Model) for the DS and FBC Overflow Parameterizations

Parameter	Symbol	Units	DS	FBC
Latitude	ϕ	°N	65	62
Sill depth	d_s	m	483	787
Channel width at d_s	W_s	km	50	15
Source water thickness at d_s	h_s	m	300	200
Entrainment depth at shelf break	d_e	m	879	985
Maximum bottom slope near shelf break	α		0.025	0.015
Bottom drag coefficient	C_d		0.003	0.003
Distance from sill to shelf break	x_{ssb}	km	100	250

topography. Dense source water at the sill depth flows across the sill, then convects downstream, and in this manner continues down the staircase topography. Unfortunately, such a descent is known to produce excessive entrainment, leading to a too-shallow penetration depth, and to contribute to the chronic shallow D_{AMOC} problem. *Wu et al.* [2007] found two solutions for the Mediterranean overflow: the PMO and cliff topography. The latter is used in CCSM4, because of its simplicity: immediately downstream of the sill grid point, the topography falls to about 2000 m, which is far below the expected penetration depth of about 1000 m. With this configuration, the Mediterranean overflow waters avoid the excess entrainment and can convect down to the expected penetration depth.

[11] The key to a general OFP is to shut off prognostic overflow by raising the topography above sill depth, as illustrated in Figure 1 by the green grid cell. In practice, this popped-up topography occurs at a minimum of three laterally neighboring grid cells, which become the source water removal sites shown in Figure 2 by the dashed arrows emanating from the source water regions labeled S upstream of both DS and FBC. These pop-ups are the only topographic differences between simulations with and without the OFP. With the OFP, source flow velocity and associated tracer fluxes are imposed as boundary conditions at the source water removal sites, as represented by the blue box in Figure 1. Similarly, the entrainment removal sites are a minimum of three neighboring grid cells at the entrainment depth. These sites are shown in Figure 2 by the dashed lines emanating from the entrainment water regions, labeled E, downstream of both DS and FBC. The entrainment velocity and tracer fluxes (brown box in Figure 1) are imposed as side boundary conditions at these sites.

[12] Also represented schematically in Figure 1 are the input parameters from the OGCM; the potential temperature and salinity of the source water at the sill depth (T_s and S_s; blue box), of the interior at the sill depth (T_i and S_i; red box), and of the entrained water at the entrainment depth (T_e and S_e; brown box). In practice, these properties are horizontal averages over the OGCM regions shown in Figure 2 as S, I, and E, respectively, for both the DS and FBC regions. Some such averaging is necessary for numerical stability, but results are not overly sensitive because horizontal gradients are much less than vertical.

[13] From these inputs, the OGCM equation of state, ρ (potential temperature, salinity, depth), is used to compute the time varying reduced gravities that drive the parameterized overflows:

$$g'_s = \frac{g}{\rho_0}(\rho(T_s, S_s, d_s) - \rho(T_i, S_i, d_s)), \tag{1a}$$

$$g'_e = \frac{g}{\rho_0}(\rho(T_s, S_s, d_e) - \rho(T_e, S_e, d_e)), \tag{1b}$$

where g is the gravitational acceleration and $\rho_0 = 1027\ \mathrm{kg\ m^{-3}}$ is a reference density. For both the DS and FBC, the radius of deformation is less than W_s and the return flow is not geometrically constrained, so the *Whitehead et al.* [1974] expression for rotating, hydraulically controlled maximum geostrophic flow through a strait gives the source overflow transport, M_s, as

$$M_s = \frac{9}{8}\frac{g'_s h_s^2}{f}, \tag{2}$$

where f is the Coriolis parameter at latitude ϕ. The PMO uses a different expression because the return flow like the source is constrained to the Strait of Gibraltar. There is nonzero source overflow only for $g'_s > 0$.

[14] Like the PMO, the *Price and Baringer* [1994] endpoint model of an entraining, rotating density current gives the entrainment transport, M_e, as

$$M_e = M_s\left(\{g'_e \mathcal{F}(\alpha, f, C_d, M_s, W_{ssb})\}^{2/3} - 1\right), \tag{3}$$

where the term in braces is a geostrophic Froude number, F_{geo}, $\mathcal{F}$ is a formal function representing the other dependencies of F_{geo} detailed in Appendix A, and W_{ssb} is the width of the overflow at the shelf break which itself is a function of M_s along with the specified parameters of Table 1. There is nonzero entrainment only for $M_s > 0$, $F_{geo} > 1$, and $g'_e > 0$.

[15] The source and entrainment transports combine to form the product water and define the entrainment parameter ϑ

$$M_p = M_s + M_e, \tag{4}$$

$$\vartheta = \frac{M_e}{M_s + M_e} = \frac{M_e}{M_p}. \tag{5}$$

From tracer conservation, the product water T and S are given by

$$T_p = T_s(1-\vartheta) + T_e\vartheta, \quad S_p = S_s(1-\vartheta) + S_e\vartheta. \tag{6}$$

A similar weighting by $(1-\vartheta)$ and ϑ gives the product water value of any tracer, e.g., ideal age described in section 5.

[16] Perhaps the most subjective, and hence model specific, piece of the OFP is the product water injection sites that define the implicit product water pathway following entrainment for each overflow. In general, for each overflow a minimum of three neighboring grid cells need to be identified for each model level below sill depth. In practice, levels need only span the depth range of the staircase topography. For example, $N_p = 8$ levels, discrete depth levels

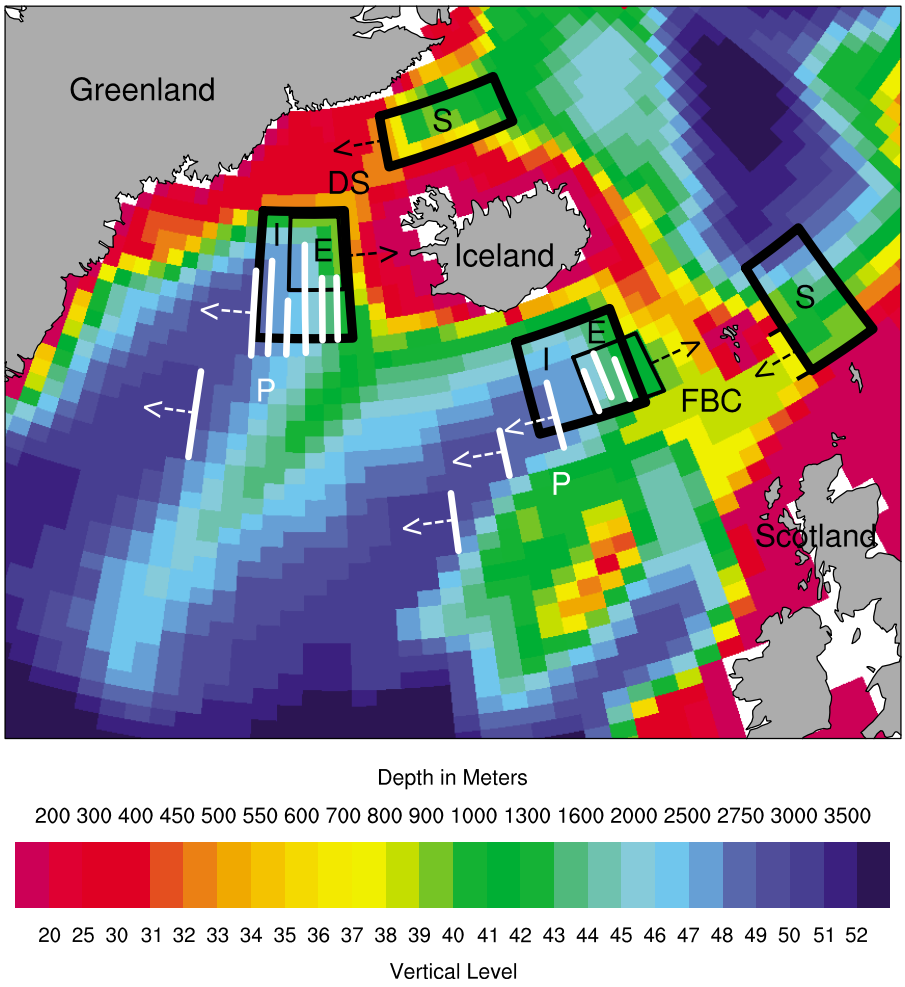

Figure 2. Bottom topography as represented in the model in the vicinity of the Denmark Strait (DS) and Faroe Bank Channel (FBC) overflows. The colors indicate the model vertical levels. The corresponding depths are given above the color bar. The boxed regions denoted by I, E, and S indicate the interior, entrainment (thin box), and source regions in the horizontal, respectively, whose T and S properties are used to compute the necessary densities. The source and entrainment box edges at which the respective water properties and transports are imposed as side boundary conditions in the OGCM are indicated by the black arrows, showing directions corresponding to flows out of the OGCM domain. The white lines denoted by P show the prespecified product water injection locations into the OGCM domain. All product water sites have the same injection direction as denoted by the white arrows drawn at only a few of the sites for clarity.

43 through 50 (see section 4 and Figure 2), suffice for both DS and FBC. Here, N_p represents the number of product water injection sites. The geographic locations of these sites are shown by the white lines in Figure 2, with dashed white arrows emanating from the deepest in the injection direction. There are only 7 DS locations and 6 FBC, because sites at adjacent levels can be at the same locations (e.g., 45 and 46 at DS, 44 and 45 as well as 46 and 47 at FBC).

[17] Determination of the product water injection site requires additional input from the OGCM; the potential temperature T_n and salinity S_n at each of the N_p product injection sites. As n increases from 1 to N_p, the associated depth d_n increases and the location moves downslope unless there is a topographic cliff (e.g., DS levels 45 and 46; n = 3 and 4). The search for the injection sites begins with $n = N_p - 1$ and ends with $n = 1$. However, the first time the condition

$$\rho(T_p, S_p, d_n) > \rho(T_n, S_n, d_n) \tag{7}$$

is satisfied, the search stops and the product water is injected through side boundary conditions at the sites corresponding to the level of depth d_{n+1}. In cases where this condition is satisfied for $n = N_p - 1$ the injection occurs at the deepest sites, as a dense bottom current that is free to flow without excessive entrainment, because of the relatively flat downstream topography shown in Figure 2. The product water injection occurs at the shallowest site when (7) is not satisfied.

[18] As detailed in Appendix A, the CCSM4 ocean model employs the common barotropic-baroclinic split method to

Table 2. DS Overflow Properties From Observations and Simulations OFP, OCN*, and CCSM*[a]

	Observations	Observation Estimates From	OFP	OCN*	CCSM*
T_s	0.25	Table of Observations from *Legg et al.* [2009][b]	0.31	0.79	2.61
	−0.4–0.7	*Macrander et al.* [2005, 2007]			
S_s	34.81	Table of Observations from *Legg et al.* [2009][b]	34.91	34.86	35.20
ρ_s	1027.94	Table of Observations from *Legg et al.* [2009][b]	1028.02	1027.95	1028.08
M_s	2.9	Table of Observations from *Legg et al.* [2009][b], *Dickson and Brown* [1994]	3.0	2.9	2.6
	3–4	*Dye et al.* [2007]			
	2.6–3.8	*Macrander et al.* [2005, 2007]			
	2.7	*Girton and Sanford* [2003]			
T_e	–		4.41	5.71	7.35
S_e	–		34.99	35.10	35.56
ρ_e	–		1027.73	1027.67	1027.81
M_e	2.3	Table of Observations from *Legg et al.* [2009][b], *Dickson and Brown* [1994]	0.7	0.8	0.7
	1.2	*Girton and Sanford* [2003]			
T_p	2.1	Table of Observations from *Legg et al.* [2009][b]	1.09	1.82	3.60
S_p	34.84	Table of Observations from *Legg et al.* [2009][b]	34.93	34.91	35.28
ρ_p	1027.85	Table of Observations from *Legg et al.* [2009][b]	1027.98	1027.91	1028.05
M_p	5.2	Table of Observations from *Legg et al.* [2009][b], *Dickson and Brown* [1994]	3.7	3.7	3.3
	3.9	*Girton and Sanford* [2003]			
d_p	>1600	Table of Observations from *Legg et al.* [2009][b]	>3000	1969[c]	1969[c]

[a] T, S, ρ, and M represent potential temperature (°C), salinity (psu), density (referenced to surface) (kg m^{-3}), and volume transport (Sv), respectively. Here d_p is the product water depth in meters. The model d_p represents the middepth of the model vertical level into which the product water is injected. The values from OCN* and CCSM* represent 10 and 30 year means, respectively.

[b] In which the DS data are based on the field campaigns described by *Girton and Sanford* [2003].

[c] Here the top and the bottom depths of this level are 1863 and 2075 m, respectively.

solve the momentum equations. Imposing volume transports as side wall boundary conditions at the source, entrainment, and product sites requires careful modifications to this method to ensure local mass (volume) conservation from which global conservation must follow. The PMO is much simpler, because mass is conserved by an inflow co-located with the source on the same vertical plane, so that there is no effect on the barotropic solution.

3. Diagnostic Assessment of the OFP

[19] A necessary test of the OFP, its numerical implementation, and the parameter choices of Table 1 is to assess whether it reproduces observed Nordic Sea overflow properties (see Appendix B and Tables 2 and 3) given observed state inputs. We note that this assessment does not test the impacts on D_{AMOC}. Here, we use the annual mean climatological T and S Polar Science Center Hydrographic Climatology (PHC2) data sets (a blending of the *Levitus et al.* [1998] and *Steele et al.* [2001] data for the Arctic Ocean) as inputs to the parameterization. The resulting overflow properties are shown in Tables 2 and 3 for DS and FBC, respectively, in the OFP column, but because these OFP T_s and S_s are averages over large volume climatologies, we do not necessarily expect them to closely match mostly local measurements in the "observations" column.

[20] In DS, in comparison with the observations, the OFP values of T_s = 0.31°C, S_s = 34.91 psu, ρ_s = 1028.02 kg m^{-3}, and M_s = 3.0 Sv (1 Sv ≡ 10^6 m^3 s^{-1}) are all in rather good agreement. However, M_e = 0.7 Sv and hence the resulting M_p = 3.7 Sv in the OFP are lower than estimates given in the Table of Observations (TO [*Legg et al.*, 2009], see Appendix B) and in the work of *Dickson and Brown* [1994], but they both compare more favorably with the lower estimates of M_e = 1.2 and M_p = 3.9 Sv from *Girton and Sanford* [2003]. As a result of low entrainment, the OFP T_p and S_p largely reflect the characteristics of the source water, and the overly dense product water penetrates below 3000 m depth.

[21] In FBC, the OFP values of T_s = −0.66°C, S_s = 34.90 psu, and hence ρ_s = 1028.06 kg m^{-3} are in excellent agreement with the observational estimates. Similarly, M_s = 2.2 Sv is within the observed ranges, supporting the model fidelity. As in DS, M_e = 0.5 Sv and hence M_p = 2.7 Sv with the OFP remain lower than the TO and *Dickson and Brown* [1994] estimated transports. However, when compared to the more recent observational mean estimates of M_e = 0.3 and M_p = 2.7 Sv at 150 km downstream of the sill from *Mauritzen et al.* [2005], the parameterized transports are in good agreement, as are T_p and S_p in OFP. The FBC product water penetrates below 3000 m depth as in DS, again in good agreement with the observations.

[22] Some averaging of T and S used for reduced gravity calculations in (1) is necessary for numerical stability, but fortunately there appears to be little impact on the OFP, and on M_e in particular. Therefore, these averaging regions (S, E, and I in Figure 2) are made quite large. Arguably, the observational entrainment transport estimates have large uncertainties due to both inherent measurement difficulties and substantial spatial and temporal variability of the overflow waters [*Mauritzen et al.*, 2005]. Nevertheless, our parameterized M_e remains mostly below these observational estimates. Such low M_e is also seen in high-resolution regional models in which the Nordic Sea overflows are explicitly resolved. For example, the FBC M_e is 0.9 Sv in the 2 km resolution model of *Riemenschneider and Legg* [2007] and the DS M_e is about 1.4 Sv in a 1/12° model used by

Table 3. Same as in Table 2 Except for the FBC Overflow Properties[a]

	Observations	Observation Estimates From	OFP	OCN*	CCSM*
T_s	0	Table of Observations from *Legg et al.* [2009][b]	−0.66	1.51	3.11
S_s	34.92	Table of Observations from *Legg et al.* [2009][b]	34.90	34.97	35.28
ρ_s	1028.07	Table of Observations from *Legg et al.* [2009][b]	1028.06	1027.98	1028.10
M_s	1.8	Table of Observations from *Legg et al.* [2009][b]	2.2	1.8	1.8
	2.1 ± 0.2	*Dye et al.* [2007]			
	1.5–3.5 (2.4)	*Mauritzen et al.* [2005]			
T_e	–		6.02	6.69	9.10
S_e	–		35.14	35.24	35.76
ρ_e	–		1027.66	1027.65	1027.70
M_e	1.5	Table of Observations from *Legg et al.* [2009][b]	0.5	0.1	0.4
	(1.2)	*Mauritzen et al.* [2005][c]			
	(0.3)	*Mauritzen et al.* [2005][d]			
T_p	3.3	Table of Observations from *Legg et al.* [2009][b]	0.55	1.79	4.10
	0–6	*Mauritzen et al.* [2005]			
S_p	35.1	Table of Observations from *Legg et al.* [2009][b]	34.94	34.98	35.36
	34.9–35.15	*Mauritzen et al.* [2005]			
ρ_p	1027.9	Table of Observations from *Legg et al.* [2009][b]	1028.03	1027.97	1028.06
M_p	3.3	Table of Observations from *Legg et al.* [2009][b]	2.7	1.9	2.2
	3.0–4.2 (3.6)	*Mauritzen et al.* [2005][c]			
	2.5–2.9 (2.7)	*Mauritzen et al.* [2005][d]			
d_p	3000	Table of Observations from *Legg et al.* [2009][b]	>3000	2187[e]	2187[e]
	>2000	*Mauritzen et al.* [2005]			

[a]The numbers in parentheses represent the average transports.
[b]The FBC data given in the Table of Observations in the work of *Legg et al.* [2009] are based on the field campaigns described by *Mauritzen et al.* [2005].
[c]Obtained at 100 km downstream of the sill.
[d]Obtained at 150 km downstream of the sill.
[e]Here the top and the bottom depths of this level are 2075 and 2298 m, respectively.

Chang et al. [2009]. The choices of α, C_d, and x_{ssb} exert considerable control on M_e, largely through their impacts on the speed and width of the downstream flow. For example, setting $\alpha = 0.03$, $C_d = 4 \times 10^{-3}$, and $x_{ssb} = 150$ km for DS and $\alpha = 0.02$ and $C_d = 4 \times 10^{-3}$ for FBC results in $M_e = 1.8$ and 1.9 Sv, respectively. However, prognostic model simulations with these parameter values eventually produce much shallower product depths due to lighter product water densities. Therefore, we have chosen to proceed with more defensible parameters and hence somewhat lower-than-observed M_e, in favor of denser and deeper-penetrating product waters. We note that another approach could be to modify directly how W_{ssb} is calculated to boost M_e, based on both observational and high-resolution model data (J. Price, personal communication). Unfortunately, this approach cannot be adopted in a climate model because such a W_{ssb} formulation is fixed in time for the present-day conditions and cannot respond to any changes in climate unlike the time-dependent form of W_{ssb} given in (A10) used in this study.

4. Numerical Model and Experiments

[23] The OFP has been implemented in the CCSM4 ocean component. It is a level-coordinate ocean model based on the Parallel Ocean Program (POP) of the Los Alamos National Laboratory [*Smith et al.*, 2010]. The present ocean model version, however, differs significantly from the one described by *Danabasoglu et al.* [2006] used in the CCSM3 simulations: the base code has been updated to POP2 and many physical and numerical developments have been incorporated. These improvements include the near-surface eddy flux parameterization of *Ferrari et al.* [2008] as implemented by *Danabasoglu et al.* [2008]; the abyssal tidal mixing parameterization of *St. Laurent et al.* [2002] as implemented by *Jayne* [2009]; the submesoscale mixing parameterization of *Fox-Kemper et al.* [2008a] as implemented by *Fox-Kemper et al.* [2008b]; modified anisotropic horizontal viscosity coefficients with much lower magnitudes than in CCSM3 [*Jochum et al.*, 2008]; and modified K-Profile Parameterization (KPP) [*Large et al.*, 1994] that uses horizontally-varying background vertical diffusivity and viscosity coefficients that are generally larger than in CCSM3 [see *Jochum*, 2009]. The model tracer equations use the *Gent and McWilliams* [1990] isopycnal transport parameterization with vertically-varying thickness and isopycnal diffusivity coefficients [*Danabasoglu and Marshall*, 2007].

[24] We use the nominal 1° horizontal resolution version of the ocean model described by *Danabasoglu et al.* [2006]. However, the number of vertical levels has been increased from 40 levels in CCSM3 to 60 levels in the present version. Most of this increase occurs in the upper ocean where the resolution is uniform at 10 m in the upper 160 m. The resolution increases to 250 m by a depth of about 3500 m, below which it remains constant. The minimum and maximum ocean depths are 30 and 5500 m, respectively. At the DS source, entrainment, and product water depths, the vertical grid resolution is about 40, 100, and 165–240 m, respectively. The corresponding vertical resolutions for the FBC are 85, 115, and 165–240 m.

[25] We have reexamined and modified the model bottom topography, considering the needs of the overflow parameterization. However, because this was our first implementation, we took a very conservative approach in our modifications some of which may not be necessary. These

changes were made (1) to ensure that there are three or more sidewall grid points at the same levels as the source, entrainment, and product sites to satisfy numerical requirements, (2) to eliminate any isolated bowls or less than two grid point channels inhibiting resolved flow in the vicinity of the source and entrainment regions, and (3) to widen some abyssal downstream choke points to allow deep product water easier access to abyssal basins. Specifically, for the DS, the region in the upstream vicinity of the source was altered to reduce the deep fall-off east of the sill. For the FBC, the entire region from the Iceland-Scotland ridge to the actual geographic FBC was widened and flattened to three grid-point wide, and a small rise was placed on its southerly edge to ensure prognostic flow would proceed in the direction of the actual geographic FBC. Some widening of a few regions in the deep product area was also done.

[26] The coupled simulations use a preliminary version of the CCSM4. The atmospheric model is based on the nominal 2° horizontal resolution, 26 vertical level, finite-volume dynamical core version of the Community Atmospheric Model (CAM) described by *Neale et al.* [2008]. The current version has some updated model physics, including a new two-moment bulk stratiform cloud microphysics scheme [*Gettelman et al.*, 2008; *Morrison and Gettelman*, 2008], a modal aerosol model (MAM) [*Ghan and Easter*, 2006; *Ghan and Zaveri*, 2007], and the Rapid Radiative Transfer Model for General circulation models (RRTMG) [*Iacono et al.*, 2008; *Mlawer et al.*, 1997]. The land model is the Community Land Model version 4 (CLM4) [*Oleson et al.*, 2010] and shares the atmosphere's horizontal grid. The basic dynamics and thermodynamics of the sea ice model is quite similar to that used in CCSM3 [*Holland et al.*, 2006; *Briegleb et al.*, 2004]. It has been updated to the CICE4 model [*Hunke and Lipscomb*, 2008]. Improvements from CCSM3 include the incorporation of a Delta-Eddington multiple scattering radiative transfer model [*Briegleb and Light*, 2007] to simulate the interactions between solar radiation and snow, sea ice, and melt ponds, and a parameterization for melt ponds that relates the pond volume to the surface melt water flux (Bailey et al., personal communication). There are also improvements to the ridging parameterization used in CCSM3, following *Lipscomb et al.* [2007]. The sea-ice model is on the same horizontal grid as the ocean model.

[27] In uncoupled ocean integrations, the surface fluxes of heat, salt, and momentum are computed using the bulk forcing method described by *Large et al.* [1997] as updated by *Large and Yeager* [2008]. We use the normal year atmospheric forcing (NYF) data sets developed by *Large and Yeager* [2004]. This data set consists of single annual cycles of all the needed fields, and can be used repeatedly without initiating any spurious transients. It has been recently proposed as common atmospheric forcing data for use in global ocean and ocean-ice simulations, i.e., Coordinated Ocean-Ice Reference Experiments [*Griffies et al.*, 2009]. A weak salinity restoring to the PHC2 data with a 4 year time scale over the top 50 m is applied globally with its global mean subtracted. We do not use an active sea-ice model in uncoupled ocean integrations. Instead, we prescribe sea-ice fraction using the observed daily climatological data set from *Comiso* [1999].

[28] We performed four experiments. OCN and CCSM are the uncoupled and coupled control cases, respectively, without the overflow parameterization. The corresponding simulations in which both the DS and FBC overflows are parameterized are denoted as OCN* and CCSM*. All cases were integrated for 170 years each, starting with the PHC2 January-mean T and S climatology and zero velocity. We note that although the integration length is not long enough for deep waters to equilibrate, it is certainly sufficient to assess the major impacts of the overflow parameterization. Unless otherwise noted, our analysis is based on year 170 for OCN and OCN*, but due to inherent interannual variability in the coupled simulations, the time mean for years 141–170 is used for CCSM and CCSM*. In the following, we compare OCN and OCN* solutions for verification of the OFP, and use CCSM and CCSM* simulations to assess its climate impacts.

5. Results

5.1. Time Evolution and Mean of the Parameterized Overflow Properties

[29] All the exchanges in parameterized overflows depend on the prognostic, i.e., time-dependent, T and S fields that themselves depend on atmospheric surface forcing and ocean model physics. For example, the source and entrained water densities and hence the final product water density and penetration depth all depend on the evolving ambient water properties. Therefore, it is important to show that the simulations with this parameterization achieve stable solutions, particularly in coupled climate experiments. This success is demonstrated for the DS and FBC overflows in Figures 3 and 4, respectively. Figures 3 and 4 present the annual mean parameterized M, T, S, and d_p time series from OCN* and CCSM* in comparison with the corresponding OFP values from Tables 2 and 3. In both simulations, the initial overflow properties after the first few time steps, as expected, are very similar to those of the OFP, but they quickly change as the ocean fields evolve. In OCN*, this initial adjustment period is about 20 years, and thereafter all the time series remain rather steady. By construction, there is no appreciable interannual variability with the NYF. The source transport and its properties could but do not have any significant drifts. However, there are small, but noticeable drifts in T_e and S_e throughout the integration period which are also reflected in T_p and S_p for both DS and FBC. In contrast, in CCSM* a rapid 10–20 year adjustment is followed by a longer adjustment period taking 70–80 years with usually larger trends than in OCN*. Thereafter, the solutions remain stable. With the exception of d_p, the CCSM* time series exhibit rich interannual variability. These interannual fluctuations in T and S are largely correlated and density compensating. Therefore, changes in ρ_p are not large enough to trigger different d_p after about year 60.

[30] At DS, the mean M_s, M_e, and M_p are very similar in OCN* and CCSM* (see also Table 2). The source transports in both, 2.9 and 2.6 Sv, respectively, are within the observational ranges. As in OFP, the entrainment transports remain lower than the observational estimates at about 0.8 and 0.7 Sv in OCN* and CCSM*, respectively. Consequently, the resulting mean M_p values are also lower than in observations, but in agreement with those of the OFP. We

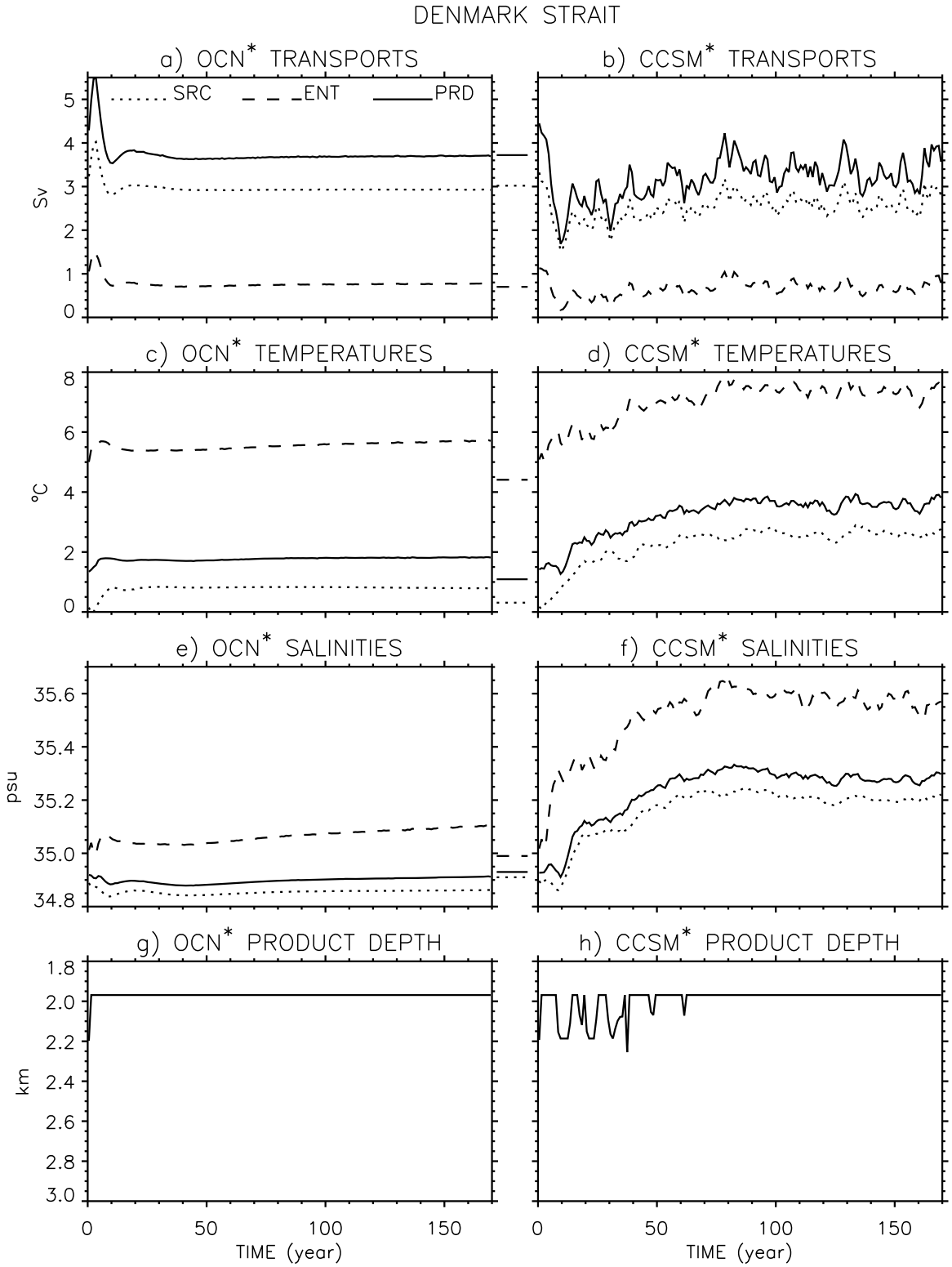

Figure 3. Time series of the annual mean DS overflow properties from OCN* (Figures 3a, 3c, 3e, and 3g) and CCSM* (Figures 3b, 3d, 3f, and 3h): (a, b) volume transports, (c, d) potential temperatures, (e, f) salinities, and (g, h) product water depth. The source (SRC, dotted lines), entrainment (ENT, dashed lines), and product (PRD, solid lines) properties are shown. The short line segments between the frames indicate the corresponding OFP values from section 3 and Table 2.

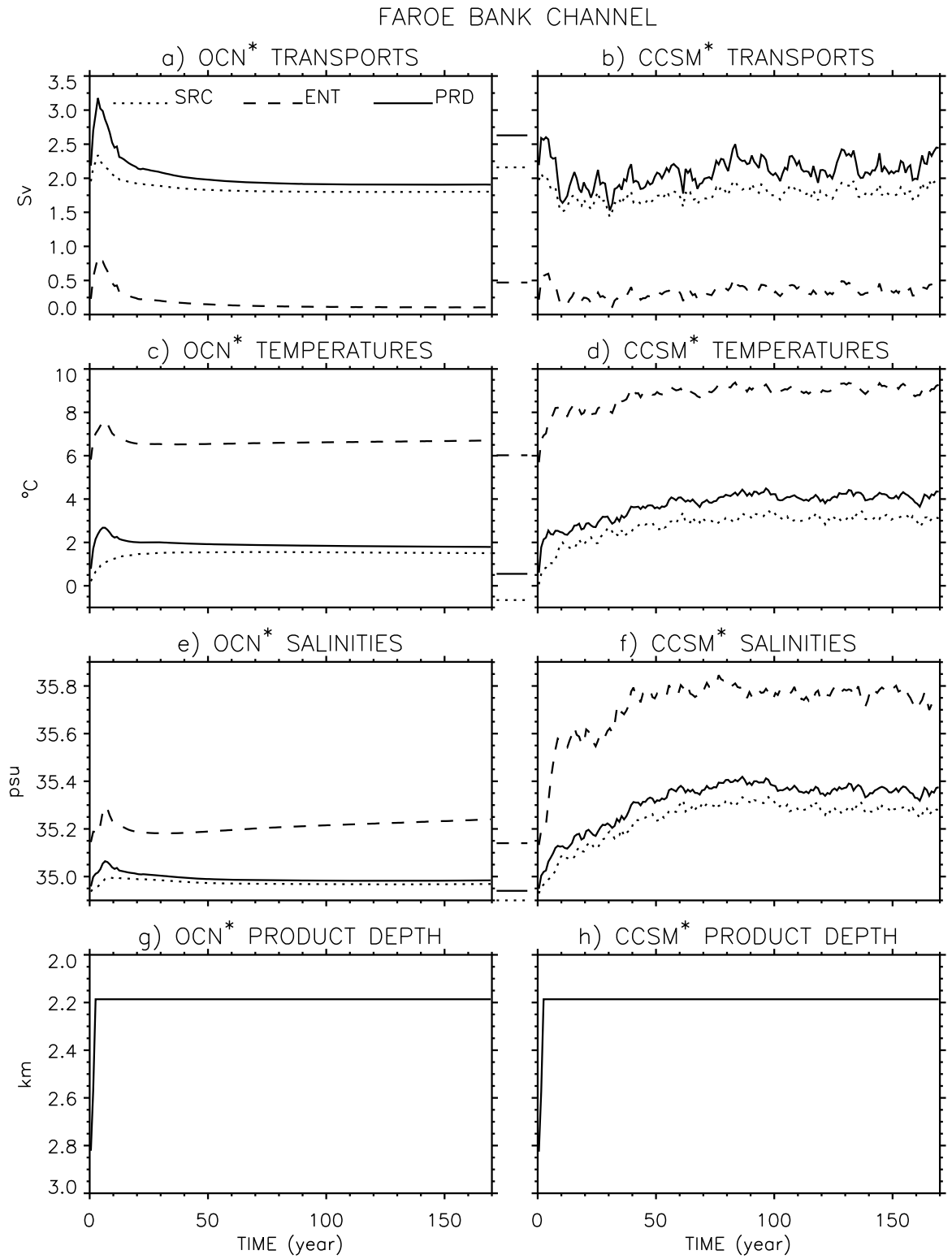

Figure 4. Same as in Figure 3 except for the FBC overflow. OFP values are from Table 3.

note a range of $2.8 \leq M_p \leq 4.2$ Sv over the last 100 years in CCSM*. The source and product water T and S in OCN* are closer to their respective observational estimates than those of CCSM*. In the latter, $S_s = 35.20$ and $S_p = 35.28$ psu are much saltier, and $T_s = 2.61$ and $T_p = 3.60$°C are warmer than those of either the observations, OFP, or OCN*. Similarly, $T_e = 7.35$°C and $S_e = 35.56$ psu in CCSM* are much warmer and saltier than in either OFP and OCN*. Consequently, these density compensating T and S biases produce mean ρ_s and ρ_p that are only somewhat larger than in observations,

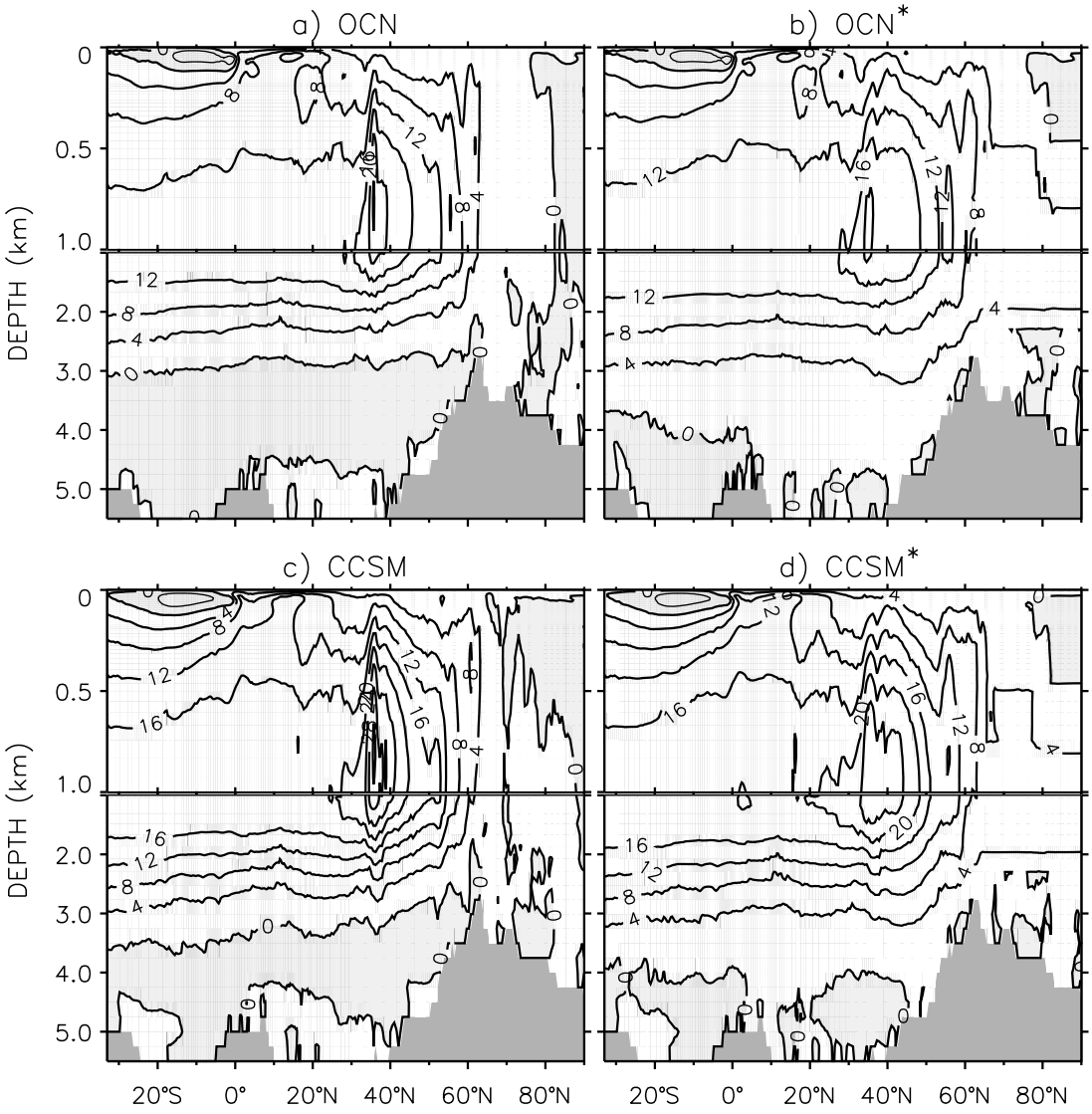

Figure 5. Time mean meridional overturning circulation in the Atlantic Ocean. The transports include the Eulerian mean and parameterized mesoscale and submesoscale contributions. The positive and negative (shaded regions) contours denote clockwise and counterclockwise circulations, respectively. The contour interval is 4 Sv.

OFP, and OCN*. In spite of these differences and differences in the ambient water T and S discussed below, the product waters are injected at a depth of 1969 m (level 46) in both OCN* and CCSM*, consistent with the observational estimates.

[31] The FBC transports in OCN* and CCSM* display very similar characteristics as the DS transports (Figures 4a and 4b and Table 3): the mean FBC M_s, M_e, and M_p are comparable in OCN* and CCSM*; in both cases, mean M_s is in good agreement with observational estimates; and in both cases, M_e and, consequently, M_p are lower than in observations. However, the M_p range of 2.0 to 2.5 Sv in CCSM* represents a smaller range than that of DS (Figures 3b and 4b). As in the DS properties, the FBC source, entrainment, and product T and S in OCN* are in much better agreement with either observational estimates or OFP than those of CCSM*. Again, in the latter, density-compensating warm and salty biases persist, but the resulting densities remain in agreement with those of the observational estimates, OFP, and OCN*. We note that S_p = 35.36 psu in CCSM* is even larger than the relatively broad observational range. Similar to the DS overflow, the product water properties and their interannual variability mostly reflect those of the source waters due to the low entrainment rates. As observed, the FBC ρ_p is larger than that of DS, with the product water penetrating deeper to 2187 m (level 47) depth in both OCN* and CCSM*. This penetration depth, however, is somewhat shallower than the observational estimate given in Table 2 despite the larger-than-observed ρ_p of the model solutions, indicating the influence of the evolving ambient stratification.

5.2. Impacts of the OFP on the North Atlantic Circulation

[32] Although the abyssal ocean takes far longer to equilibrate in general, the features discussed here are well

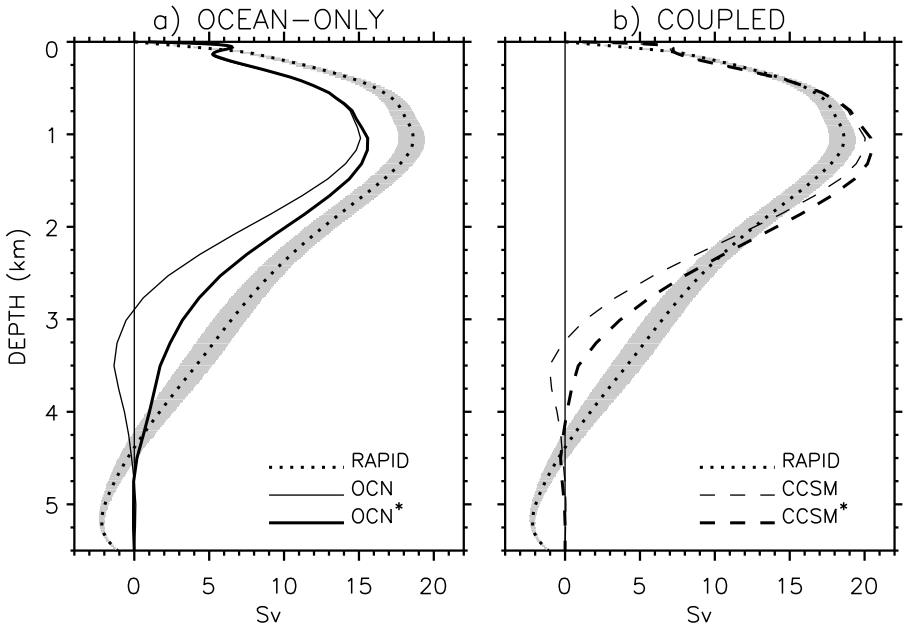

Figure 6. Time mean Atlantic meridional overturning circulation profiles at 26.5°N from (a) ocean-only and (b) coupled simulations in comparison with the 4 year mean RAPID data (April 2004 to April 2008). The shading indicates the interannual variability range in the annual mean RAPID data over the 4 years.

established and the differences remain robust among cases after only 70 to 100 years of integration. Arguably, the most significant impact of the overflow parameterization is seen in the AMOC given in Figure 5, clearly showing that the NADW penetrates much deeper with the OFP than in the control simulations. In Figure 5, the AMOC is plotted for the total flow, i.e., Eulerian-mean, parameterized mesoscale and submesoscale eddy contributions are all included, but the latter two are almost negligible. To quantify this major improvement, we present comparisons of the model AMOC profiles obtained at 26.5°N with the profile based on the RAPID data in Figure 6. Such profiles represent the total integrated transport between the surface and a given depth, and they must equal zero at the model bottom by construction in the absence of any mass sources and sinks at this latitude. In addition, the negative and positive slopes indicate northward and southward flows, respectively. Following a common interpretation of such profiles, D_{AMOC} is defined as the depth where a profile indicates a zero crossing, separating the NADW cell from that of the Antarctic Bottom Water (AABW) occupying the deeper depth levels. In OCN*, D_{AMOC} = 4650 m is in remarkably good agreement with the RAPID profile which has an interannual range of $4200 \le D_{AMOC} \le 4500$ m (Figure 6a). With D_{AMOC} = 2900 m, the NADW penetration depth is clearly much too shallow in OCN. We also note that the OCN* transport profile compares much more favorably with the RAPID profile than that of OCN between 1000 and 4500 m depth. The improvement in D_{AMOC} appears to be rather robust as evidenced also in coupled simulations (Figure 6b) where D_{AMOC} = 4100 m in CCSM* is deeper than that of CCSM (D_{AMOC} = 3200 m) in quite good agreement with the RAPID data (D_{AMOC} = 4350 m). The RAPID data show a mean bottom northward transport of the AABW and a return flow between D_{AMOC} and 5250 m. This circulation is displaced to much shallower depths in OCN and CCSM and is largely missing in OCN* and CCSM*. The improved NADW penetration depth with the OFP exposes deficiencies of the model bottom topography in representing the Romanche and Vema Fracture Zones through which the majority of the AABW spreads into the North Atlantic.

[33] The maximum northward transports across 26.5N differ very little between OCN and OCN*, i.e., 15.0 versus 15.6 Sv, respectively (Figure 6a). The corresponding RAPID transport estimate has a mean of 18.7 Sv with a standard deviation of ±5.6 Sv of daily estimates [*Cunningham et al.*, 2007], thus indicating that the model transports are within this observed standard deviation range. The corresponding transports are 20.0 and 20.5 Sv in CCSM and CCSM*, respectively, both higher than in uncoupled cases, but within the observational range. Although there is little sensitivity of the above transports to the OFP, the maximum NADW transport diminishes from 24.6 Sv in OCN to 21.0 Sv in OCN* and from 32.8 Sv in CCSM to 27.8 Sv in CCSM* (Figure 5).

[34] The D_{AMOC} differences between OCN and OCN* discussed above primarily reflect the changes in the Deep Western Boundary Current (DWBC) due to the OFP. To show this striking impact of the OFP on the DWBC, we present the horizontal velocity vectors in the northwestern Atlantic at a depth of 3876 m from OCN and OCN* in Figure 7. In OCN*, the flow out of the Labrador Sea basin moves southward off of Grand Banks and continues its well defined, southward path as the lower extension of a DWBC, hugging the North American continent. In contrast, in OCN the southward flowing DWBC is confined to shallower depths (e.g., Figure 6a) and there is a northward flowing current that becomes weaker, but still remains northward, as it enters the Labrador Sea basin at 3876 m. These differences between the two cases in the DWBC have implica-

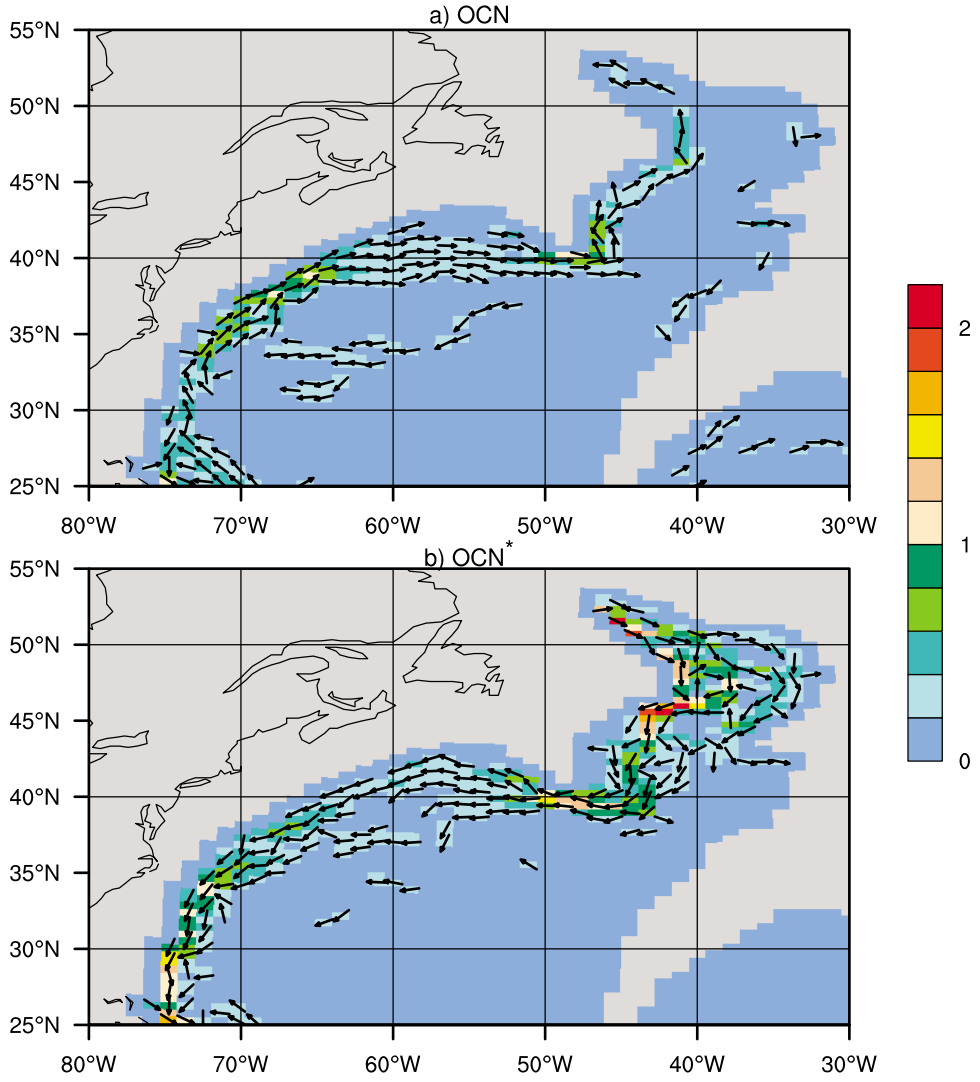

Figure 7. Time mean horizontal velocity at a depth of 3876 m from (a) OCN and (b) OCN*. Arrows and colors give the flow direction and magnitude in cm s^{-1}, respectively. Arrows are plotted only for speeds larger than 0.2 cm s^{-1}.

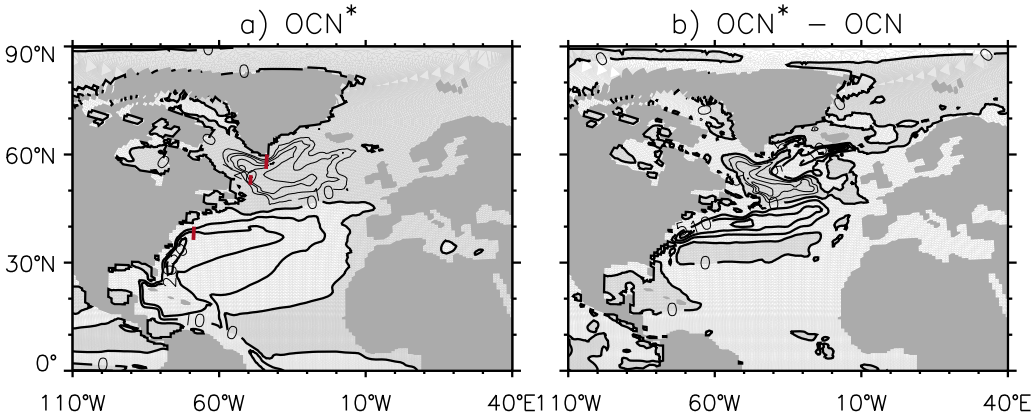

Figure 8. Time mean barotropic streamfunction (a) from OCN* and (b) its difference from OCN. The contour intervals are 10 and 5 Sv in Figures 8a and 8b, respectively. In Figure 8a, he thick and thin (shaded regions) lines indicate clockwise and counterclockwise circulations, respectively. In Figure 8b, shading and thin lines denote negative differences. Red line segments in Figure 8a denote the transport sections used in Table 4.

Table 4. Volume Transports in Sv Across the Sections Indicated in Figure 8[a]

Case	44°W Westward	49.3°W Eastward	49.3°W $\sigma_0 \geq$ 27.74 Eastward	69°W Westward
OCN	5.3	3.5	17.3	0.2
OCN*	10.7	9.3	26.7	2.0
OBS	13.3	14.7	26±5	12.5

[a]Except for the 49.3°W $\sigma_0 \geq 27.74$ column, all transports are for $\sigma_0 \geq 27.80$ kg m^{-3}. OBS represents observational estimates as follows: the 44°W section corresponds to the Cape Farewell transport from *Dickson and Brown* [1994]; the 49.3°W and 69°W sections are approximations to the 53°N and 70°W lines of *Fischer et al.* [2004] and *Joyce et al.* [2005] lines, respectively. Approximate flow directions are also noted.

tions for the near surface circulation patterns as well as the depth integrated barotropic streamfunction (BSF) as shown in Figure 8. Unfortunately, the more realistic DWBC depth in OCN* adversely affects the Gulf Stream separation location, extending it further north to Newfoundland. As discussed by *Yeager and Jochum* [2009], the relationships between the DWBC, Gulf Stream and North Atlantic Current (NAC) separation, and Labrador Sea basin properties are rather complex and improvements in any one aspect, such as the DWBC depth, does not necessarily lead to overall improvements in model solutions (see also *Spall* [1996] for DWBC and Gulf Stream interaction). There is an associated northward shift of the NAC in OCN* compared to that of OCN. As a consequence, the Northern Recirculation Gyre, which is already rather weak in OCN, is absent in OCN*. Figure 8 also shows that the circulation associated with the subpolar gyre is stronger in OCN* than in OCN by as much as 10 Sv.

[35] Table 4 presents the time mean volume transports normal to the 44°, 49.3°, and 69°W longitude lines chosen to provide quantitative comparisons with the observational transport estimates obtained approximately along these sections (see red line segments in Figure 8). We note that these sections are well downstream of the overflow sites and that the transports are based on the resolved flows which only indirectly include the contributions from the injected parameterized product waters. At Cape Farewell, the westward flow along the sloping bottom in OCN is rather anemic below 2500 m depth, i.e., mostly less than 0.5 cm s^{-1} (not shown). In contrast, this flow in OCN* is significantly stronger with velocity magnitudes in excess of 5 cm s^{-1} (not shown) and carries higher (by as much as 0.06 kg m^{-3}) density waters than in OCN. As a result of these larger velocities in OCN*, the westward volume transport for $\sigma_0 \geq$ 27.80 kg m^{-3} is 10.7 Sv, about twice as large as in OCN, and compares much more favorably with the observational estimate of 13.3 Sv from *Dickson and Brown* [1994]. At the Labrador Sea exit at 49.3°W, both cases show southward flow (not shown). However, in OCN*, the velocity magnitudes are broadly larger with especially stronger deep flows. Again, these flows carry denser waters in OCN* than in OCN by as much as 0.06 kg m^{-3}. Table 4 clearly shows the improvements in the volume transports with the OFP at this section. In particular, the OCN* transport of 26.7 Sv is in excellent agreement with the observational estimate of 26 ± 5 Sv for $\sigma_0 \geq 27.74$ kg m^{-3} from *Fischer et al.* [2004]. Further south at 69°W section, in contrast with the northeastward flow of OCN below about 2500 m depth, a southwestward flowing DWBC is clearly present in OCN* (Figures 9a and 9b). Although this increases the southwestward volume transport to 2 Sv in OCN* from 0.2 Sv in OCN and represents a modest improvement, the transport remains smaller than the observational estimate. We note that there are no appreciable differences in deep densities between the two cases at this section.

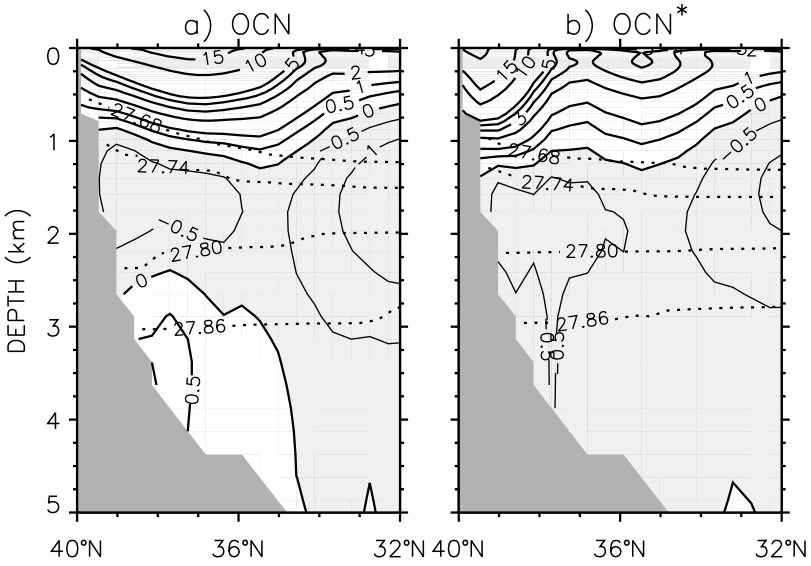

Figure 9. Time mean zonal velocity across 69°W in the North Atlantic from (a) OCN and (b) OCN*. The thin contour lines (shaded regions) indicate westward flow. The contour levels are 0, ±0.5, ±1, ±2, ±3, ±4, ±5, ±10, ±15, and ±30 cm s^{-1}. The dotted lines show the potential density (referenced to surface) with a contour interval of 0.06 kg m^{-3} for $\sigma_0 \geq 27.68$ kg m^{-3}.

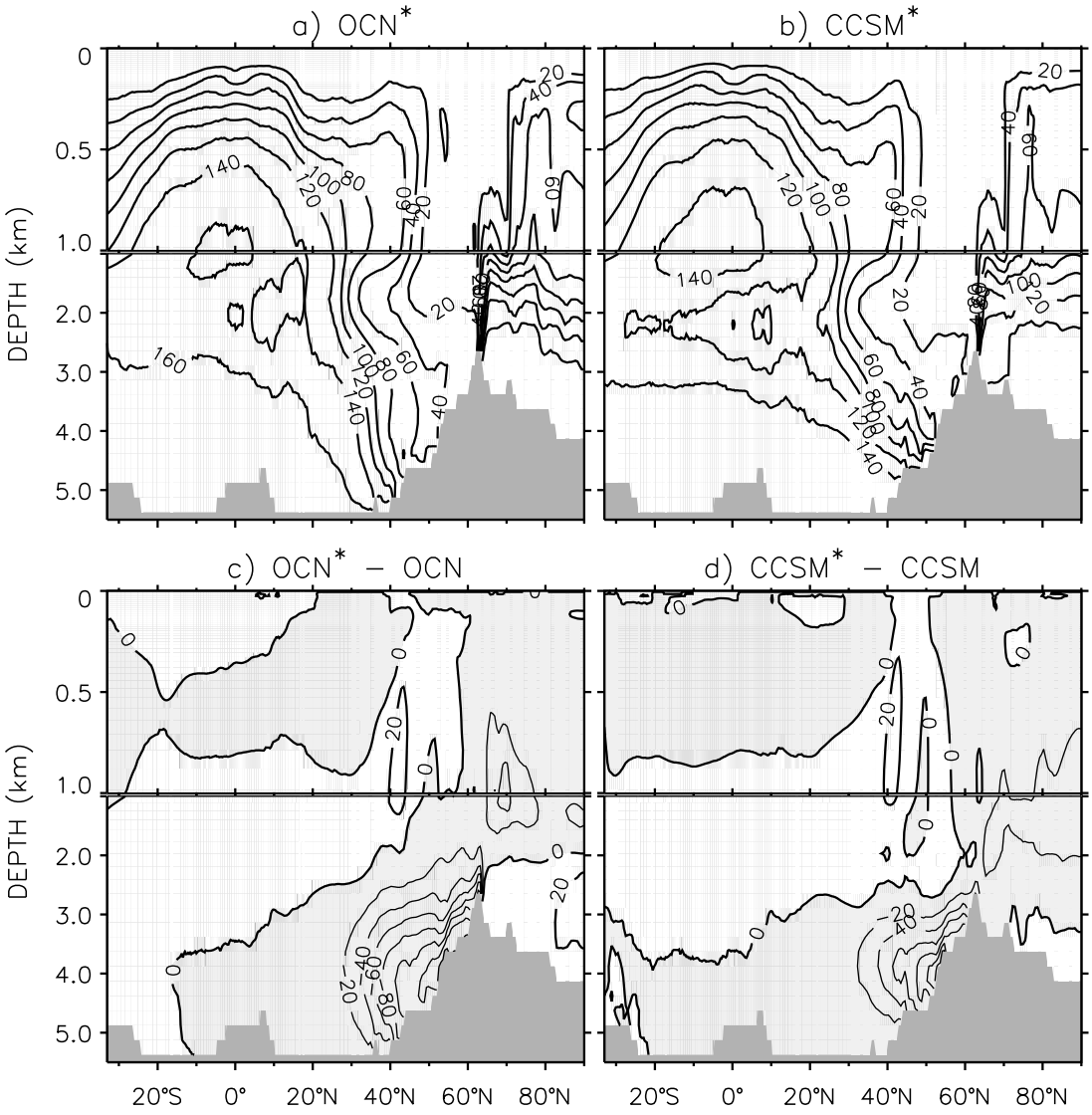

Figure 10. Time and zonal mean ideal age for the Atlantic and Arctic oceans, including the Labrador and GIN seas: (a) from OCN*, (b) from CCSM*, (c) OCN*-OCN difference, and (d) CCSM*-CCSM difference. The contour interval is 20 years. The thin lines and shading indicate negative differences (Figures 10c and 10d).

5.3. Changes in the Ventilation and Tracer Distributions in the Atlantic Basin

[36] To evaluate changes in oceanic ventilation time scales resulting from the deeper penetration of the NADW with the OFP, we consider the ideal age tracer [*Thiele and Sarmiento*, 1990]. This tracer uses the same equations as T and S, but increases by 1 for each model year. All cases are initialized with zero age, and the ideal age tracer is set to zero at the ocean surface. Thus, the regions of low ventilation have the oldest waters while the younger waters indicate recent contact with the ocean surface. Figure 10 presents the time and zonal mean ideal age distributions for the Atlantic and Arctic oceans from OCN* and CCSM* in comparison with OCN and CCSM, respectively. The difference distributions (Figures 10c and 10d) clearly show the increased ventilation of the deep North Atlantic. Indeed, the ideal ages are younger by up to 140 and 120 years, respectively, in OCN* and CCSM* with the OFP compared to the respective control cases. The upstream Nordic Sea and Arctic basins ideal ages also get younger down to about 2000 m in OCN* and 3000 m in CCSM*.

[37] There are no measurements of ideal age, so to assess if changes represent improvements, we next calculate the root mean square (rms) model minus observations difference profiles for T and S (Figure 11) downstream of the overflow regions for the Labrador Sea, North Atlantic, and South Atlantic, because the largest direct impacts of the OFP are seen in these basins. Here, the Labrador Sea region is bounded in the south and east roughly by the 50.5°N and 46°W lines, respectively; the North Atlantic basin is north of the equator, excluding the Labrador Sea and Greenland-Iceland-Norwegian (GIN) seas; and the South Atlantic basin extends south from the equator to about 34°S. We note that because the North and South Atlantic basins represent 11% and 7% of the global ocean volume, respectively, any T and

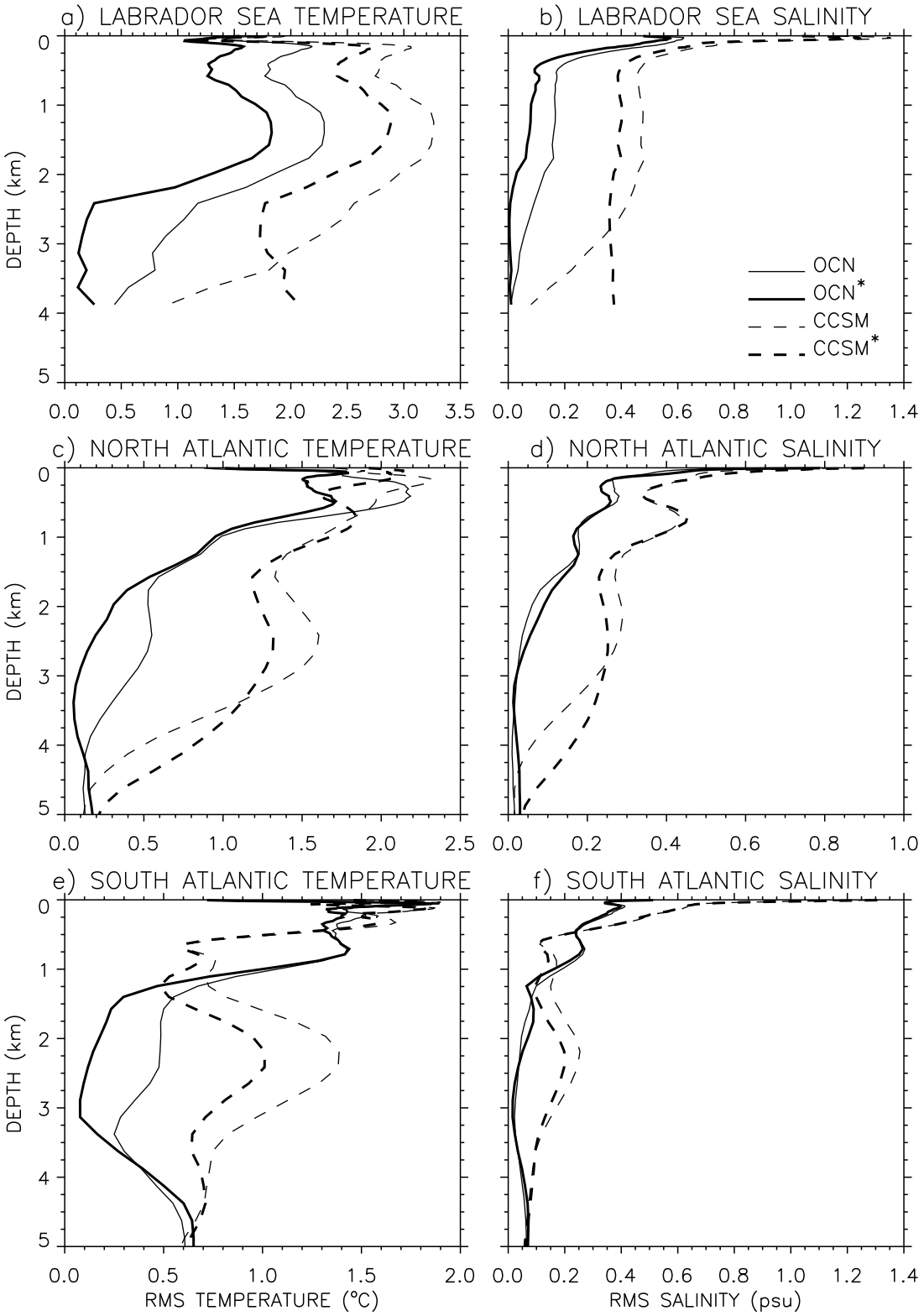

Figure 11. Root mean square (rms) model-observations difference profiles for time mean potential temperature (Figures 11a, 11c, and 11e) and salinity (Figures 11b, 11d, and 11f) in the (a, b) Labrador Sea, (c, d) North Atlantic, and (e, f) South Atlantic.

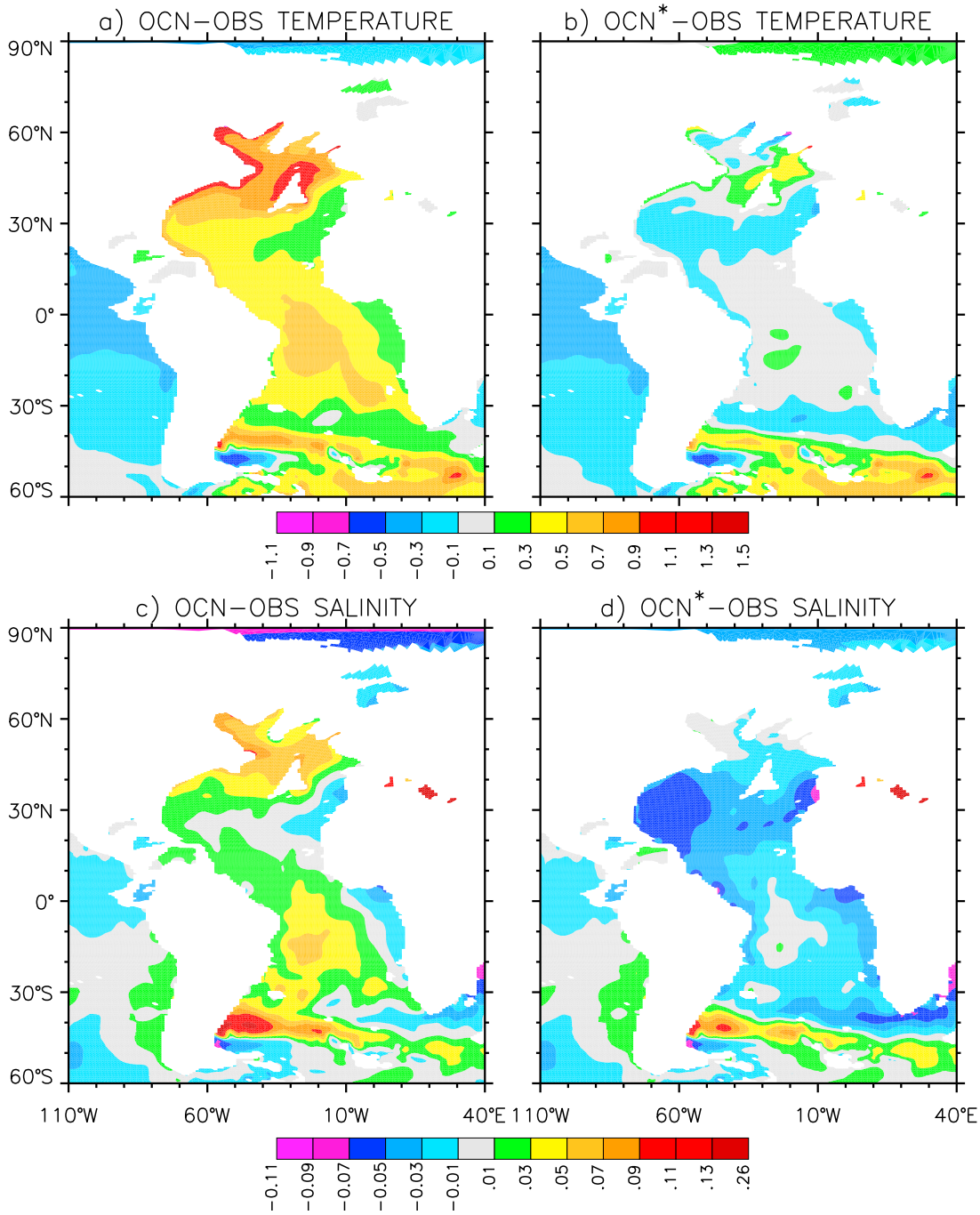

Figure 12. Time mean model minus observations (OBS) difference distributions at a depth of 2649 m for the Atlantic Ocean from the uncoupled simulations: (a) OCN-OBS potential temperature, (b) OCN*-OBS potential temperature, (c) OCN-OBS salinity, and (d) OCN*-OBS salinity differences. OBS represents a blending of the *Levitus et al.* [1998] and *Steele et al.* [2001] data sets. The potential temperature and salinity units are °C and psu, respectively.

S changes in these basins indicate larger contributions to their global integrals compared to comparable magnitude changes in the Labrador Sea, accounting for <0.3% of the global ocean volume. Figure 11 shows that the rms differences are much smaller in the uncoupled simulations than in the coupled cases at all depths except at around 1000 m depth in the South Atlantic. The larger rms error suggests deficiencies in the coupled model surface fluxes.

[38] In these basins, there are significant improvements in *T* throughout most of the water column in OCN* compared to OCN (Figures 11a, 11c, and 11e). In particular, between 1500 and 4000 m depth in the North Atlantic and within 1000–3500 m depth in the South Atlantic, the depth ranges that include pathways of the injected overflow waters, the OCN* rms differences are much smaller than in OCN. For example, they are reduced from 0.52 to 0.14°C in the North

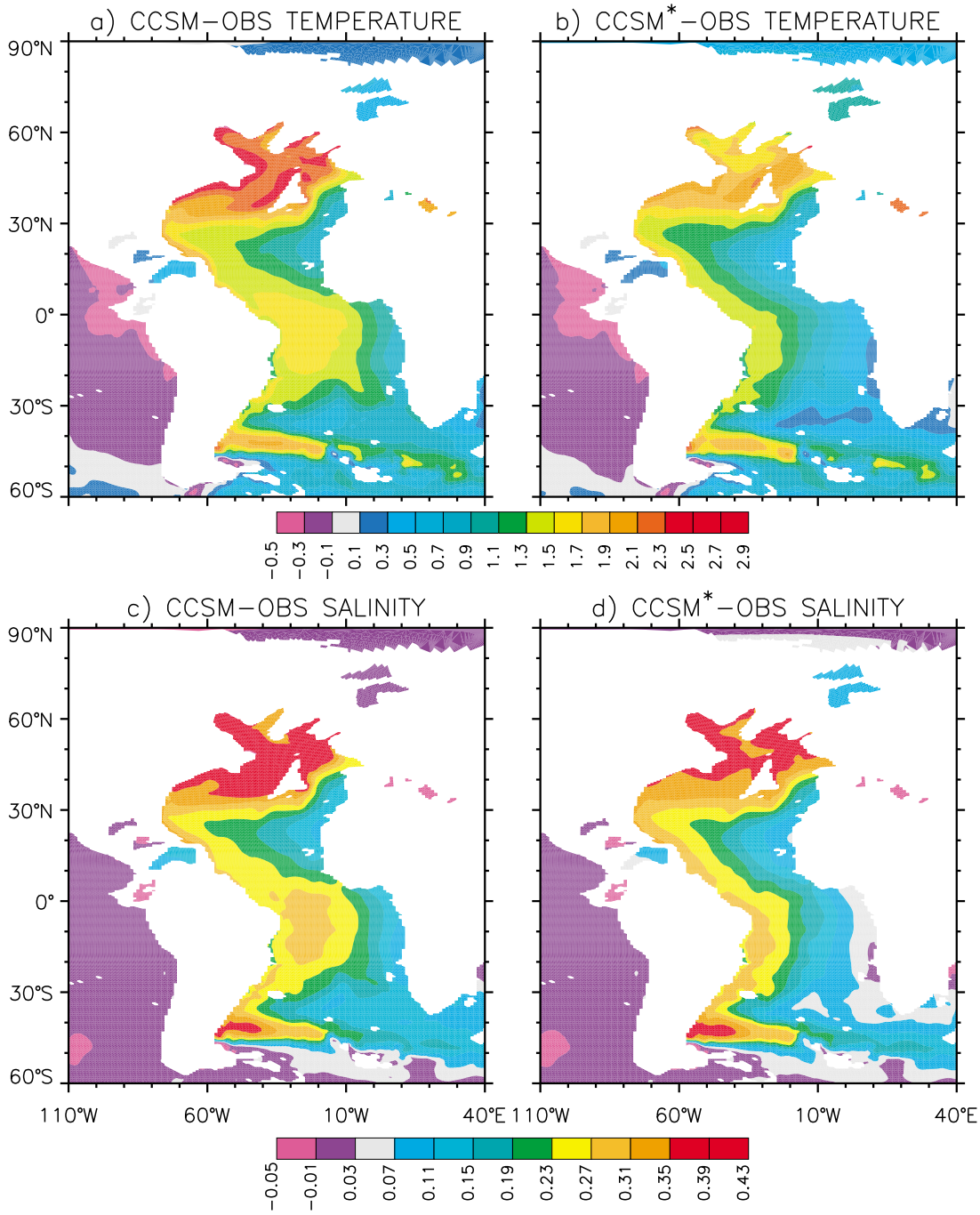

Figure 13. Same as in Figure 12 except from the coupled simulations.

Atlantic and from 0.43 to 0.10°C in the South Atlantic at a depth of 2649 m. In comparison to CCSM, there are also substantial improvements in the Labrador Sea, North Atlantic, and South Atlantic especially at the product water depth ranges in CCSM*. Again, at a depth of 2649 m, the rms T differences are reduced from 1.59 to 1.31°C in the North Atlantic and from 1.28 to 0.93°C in the South Atlantic.

[39] The salinity rms errors are already rather small in OCN at depth (Figures 11b, 11d, and 11f). In OCN*, there are further improvements in the Labrador Sea, and no appreciable differences occur elsewhere. In CCSM*, while there are some improvements in the South Atlantic, the signal is mixed in the Labrador Sea and North Atlantic. For example, in the latter basin, the CCSM* rms improves between 1000 and 2500 m depth, but is worse farther down.

[40] As typical examples of the impacts of the OFP on the spatial distributions of T and S at the product water pathway levels in the Atlantic Ocean, we show their distributions at a depth of 2649 m from OCN and OCN* in comparison with observations in Figure 12. The warm bias of OCN has been uniformly reduced in OCN*. Indeed, for the Atlantic Basin at

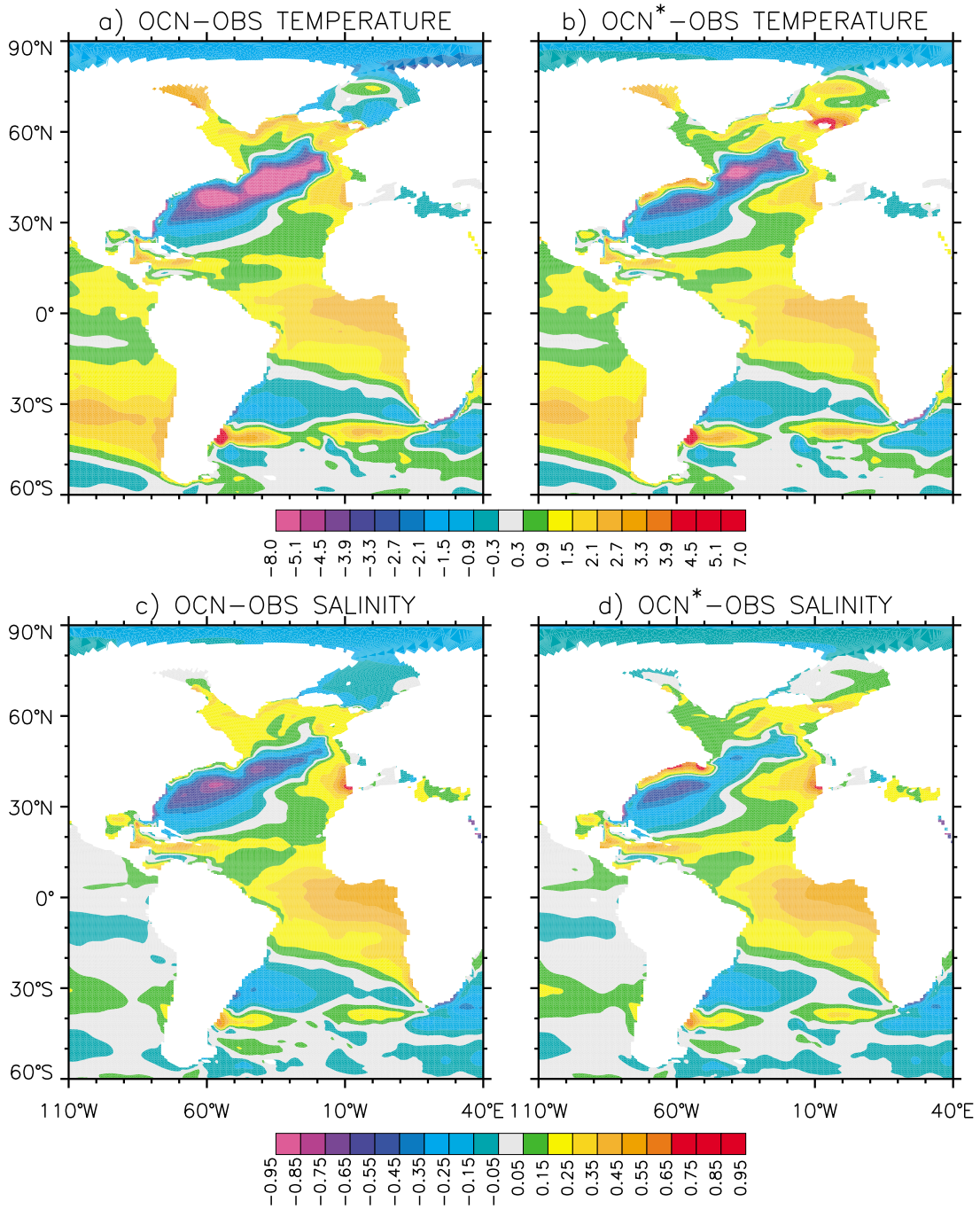

Figure 14. Same as in Figure 12 except at a depth of 409 m.

this depth, including its Southern Ocean sector and the Labrador Sea, we calculate the mean differences from observations as 0.42 and 0.01°C for OCN and OCN*, respectively. Similarly, the OFP reduces the model-observations rms bias from 0.48°C in OCN to 0.20°C in OCN*. Arguably, the largest effects of the OFP on *T* are revealed in the northern North Atlantic, particularly in the Labrador Sea and around the Grand Banks where the OCN warm bias of >1.1°C is reduced to about 0.1°C in OCN*, consistent with the altered DWBC flow in the latter. In *S*, the uniform, but small salty bias of OCN with a mean of 0.020 psu is now a small, uniform fresh bias of the same magnitude in OCN* (Figures 12c and 12d). Similarly, the rms differences from observations remain identical at 0.034 psu in both cases. As in *T*, there are important reductions in the salinity errors in the northern North Atlantic, especially in the Labrador Sea where the salty bias of >0.05 psu in OCN is virtually eliminated in OCN*. Substantial reductions of the warm and salty biases that exist in OCN in the vicinity of the Brazil-Malvinas confluence region are largely due to the southward flow of the colder and fresher overflow waters in OCN*, indicating their remote influences.

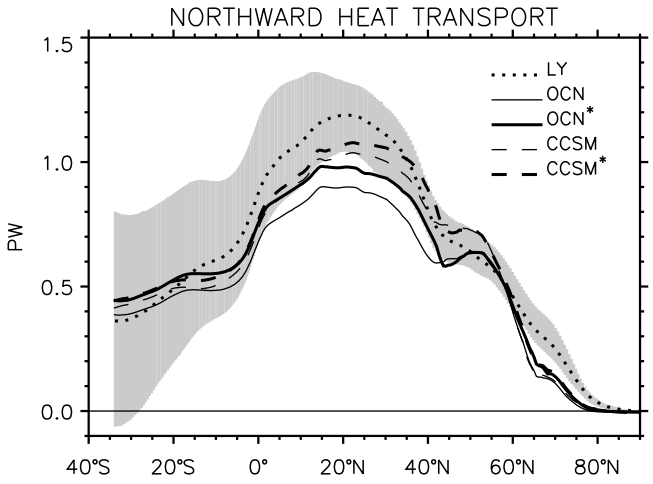

Figure 15. Time mean northward heat transport in the Atlantic Ocean. The transports include the Eulerian mean and parameterized mesoscale and submesoscale advective contributions. The dotted line denoted by LY represents implied transport calculated by *Large and Yeager* [2008] with shading showing the implied transport range in individual years.

[41] The corresponding distributions from CCSM and CCSM* are presented in Figure 13. In CCSM*, the Atlantic Basin is uniformly colder and fresher than in CCSM, thus producing more favorable comparisons with observations. Indeed, the mean differences from observations are reduced from 1.29°C in CCSM to 1.02°C in CCSM*. Similarly, the model-observations rms is down from 1.39°C in CCSM to 1.13°C in CCSM*. These represent about 20% improvements in both measures. The mean and rms salinity differences from observations are about 0.187 and 0.215 psu, respectively, in CCSM* indicating about 10% reduction in these measures compared to those of CCSM. Particularly in the northern North Atlantic, the T and S biases are lower by up to 1°C and 0.04 psu in CCSM* than in CCSM. Despite these improvements in CCSM*, however, the T and S biases in coupled simulations still remain much larger than in uncoupled cases (Figure 12 versus Figure 13).

[42] The impacts of the upper-ocean circulation changes on the model T and S distributions with the OFP are given in Figure 14 in comparison with the observations, considering only the uncoupled simulations. These are obtained at a depth of 409 m, a level at which some of the compensating upper-ocean inflow from the North Atlantic into the Nordic Sea occurs. Figure 14 shows that most of the changes are confined to the north of 20°N, especially along the NAC path and in the Subpolar Gyre. In comparison with OCN, there are significant reductions of the most prominent cold and fresh biases that occupy much of the North Atlantic between 80°W–15°W and 20°N–60°N in OCN*. For example, the minimum cold bias diminishes from −7.9°C in OCN to −6.1°C in OCN*. Unfortunately, these improvements occur at the expense of new warm and salty biases along a narrow path just off the North American coast, southeast of Grand Banks, due to more northward penetration of the Gulf Stream with the OFP. There are >0.6°C and >0.1 psu bias reductions in the Labrador Sea with the OFP. The Nordic Sea, in general, gets warmer and saltier. While the former creates further departures from observed, the latter represents an improvement. We calculate the mean T and S differences from observations for the North Atlantic between 20°N–80°N as −0.70 versus −0.08°C and −0.056 versus 0.024 psu for OCN and OCN*, respectively. The corresponding model-observations rms values are 2.39 versus 1.76°C and 0.277 versus 0.229 psu for OCN and OCN*, respectively. All these mean and rms differences indicate modest improvements in model solutions at this depth with the OFP.

[43] Figure 15 presents the total northward heat transport (NHT) in the Atlantic Ocean from all cases in comparison with the implied transport from *Large and Yeager* [2008] calculated using the CORE interannual fluxes for the 1984–2006 period. Both OCN* and CCSM* show larger NHT at nearly all latitudes than in the corresponding control experiments. Particularly in OCN*, this increase significantly improves the comparison with the implied transport estimate. The maximum NHT increases from 0.90 PW in OCN to 0.98 PW in OCN* and from 1.04 PW in CCSM to 1.08 PW in CCSM*. These represent about 10% and 4% increases in the transports with the OFP in uncoupled and coupled cases, respectively. In comparison with the control experiments, the larger NHT with the OFP occurs despite the lower NADW maximum transports, and it is primarily due to the increased potential temperature contrast between the upper- and deep ocean in both OCN* and CCSM*. For example, the northward branch of the NADW cell transports warmer (Figure 14) waters while its southward branch advects colder (Figure 12) waters in OCN* in comparison with OCN. Secondary contributions to the increased NHT come from slightly higher NADW transports south of about 30°N in the overflow cases compared to the corresponding control experiments.

5.4. Climate Impacts of the OFP

[44] The climate impact of the OFP will be through changes in SSTs, subsequently impacting the air-sea fluxes in the North Atlantic and thus affecting the overlaying atmosphere. Following *Large and Danabasoglu* [2006], the SST and surface heat flux (SHF) coupling strength, C, can be written as

$$C = \frac{\partial \mathrm{SHF}}{\partial \mathrm{SST}} = -(5 + 4V) \tag{8}$$

where V is the wind speed in m s^{-1}. C is typically 30 W m^{-2}°C^{-1} in uncoupled experiments, representing a 30 W m^{-2} increase (decrease) in SHF for a SST decrease (increase) of 1°C. However, in coupled simulations, C is about half of the above value because changes in near-surface air temperature and humidity usually produce compensating changes in the SHF response.

[45] We show the time mean SST and SHF distributions in the North Atlantic from CCSM* along with their differences from those of CCSM and observational data sets in Figure 16. Figure 16c reveals that significant CCSM*-CCSM SST differences are confined to the north of 30°N. The largest differences (>5°C) occur off the North American coast and are associated with the northward displacement of

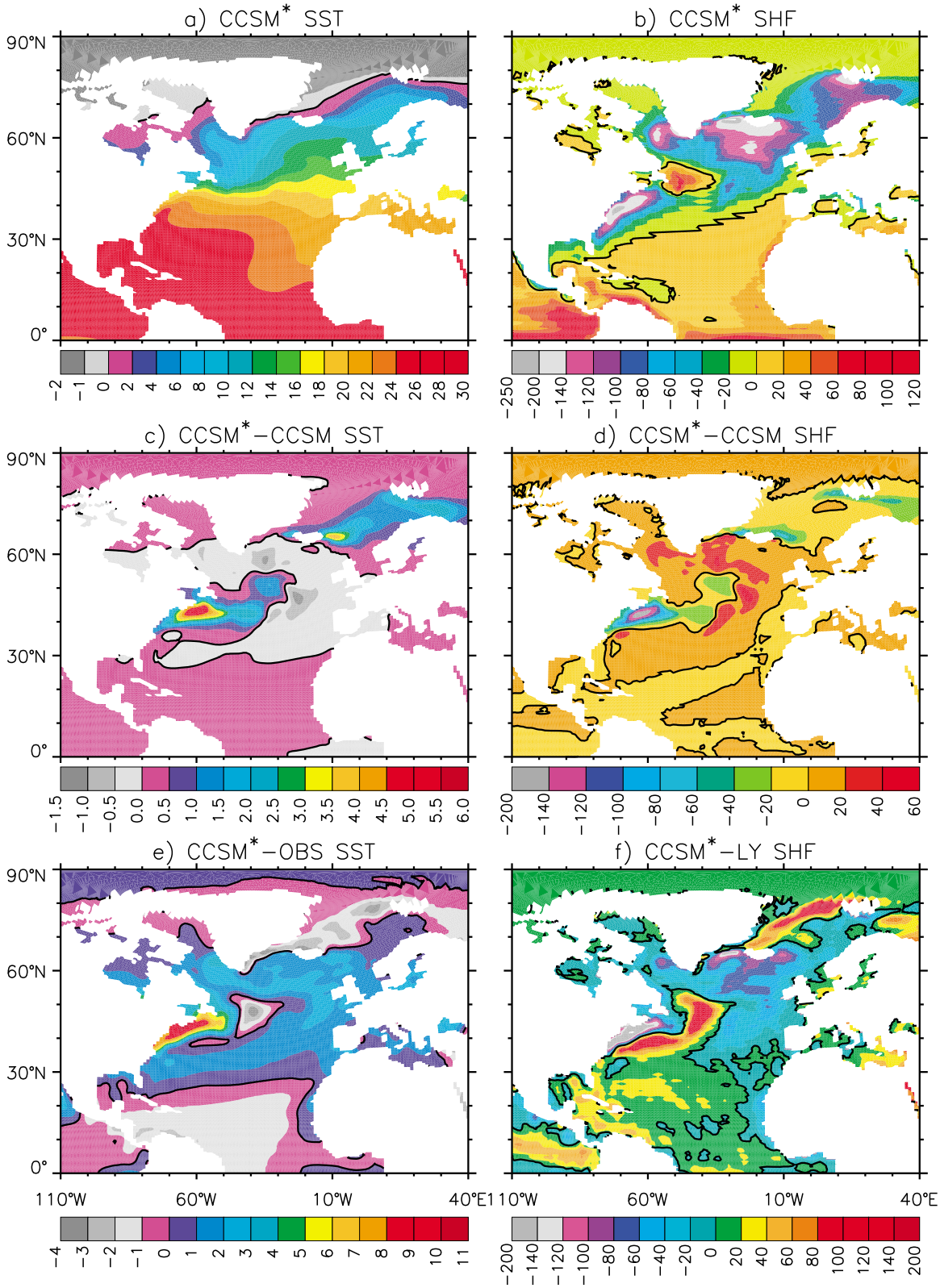

Figure 16. Time mean (a) sea surface temperature (SST) and (b) surface heat flux (SHF) from CCSM*. Their respective differences from (c, d) CCSM and (e, f) observationally based data sets are given. The SST and SHF units are °C and W m^{-2}, respectively. The zero contour lines are shown. OBS and LY refer to the *Hurrell et al.* [2008] and *Large and Yeager* [2004] data sets, respectively.

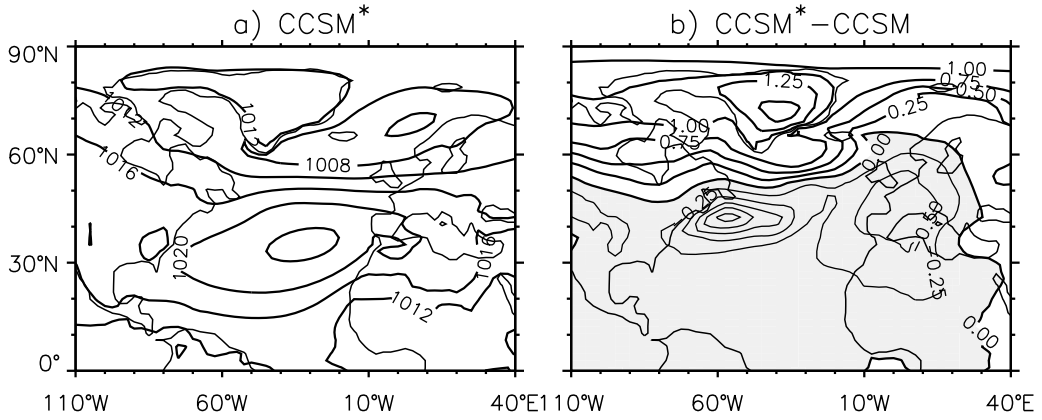

Figure 17. Time mean sea level pressure (a) from CCSM* and (b) its difference from CCSM plotted on the atmospheric grid. The contour intervals are 4 and 0.25 mbar in Figure 17a and 17b, respectively. In Figure 17b, shading and thin lines denote negative differences.

the NAC in CCSM* compared to that of CCSM (not shown). This positive difference region extends in a northeasterly direction to the middle of the Atlantic basin. The CCSM* SSTs are also warmer than in CCSM in the Nordic Sea. Particularly along a band between Iceland and Spitsbergen, SSTs are warmer by more than 1°C, exceeding 2°C just south of Spitsbergen and 3.5°C just east of Iceland. Elsewhere north of 30°N, the SSTs are generally cooler in CCSM* than in CCSM, locally reaching 1°C only in a couple of regions. The CCSM*-CCSM SHF difference distributions (Figure 16d) clearly indicate that the SHF largely responds to the above SST changes and acts to dampen them. For example, off the North American coast, the SHF reduces by more than 140 W m^{-2} to diminish the warmer SSTs there, implying a large coupling strength of about −25 W m^{-2}°C^{-1}. Even stronger coupling of about C = −40 W m^{-2}°C^{-1} occurs in the regions with −1°C SST differences. We note that in a few small regions, e.g., southwest of Spitsbergen, northern Labrador Sea, and west of the Iberian Peninsula, the coupling reverses sign and the SHF changes actually reinforce the SST changes. This implies remote effects of oceanic changes on the atmosphere. Figures 16e and 16f present the CCSM* SST and SHF differences, respectively, from the corresponding observationally based data sets. With the exception of the warmer SSTs and the associated negative SHF difference off the North American coast, these comparisons represent improvements, i.e., reducing coupled model biases, compared to the solutions from CCSM. Despite these improvements, the model-observations SST and SHF differences still remain large.

[46] The SST changes with the OFP discussed above lead to the sea level pressure (SLP) differences between CCSM* and CCSM given in Figure 17. The SLP difference has a pattern reminiscent of the negative phase of the North Atlantic Oscillation, but with much weaker magnitudes. In response to the warmer SSTs off the North American coast in CCSM*, the SLP is reduced by more than 1 mbar. These differences in the SLP diminish the strength of the time mean westerly wind stress in the 45°–60°N latitude band in the North Atlantic by up to 15% in CCSM* compared to that of CCSM (not shown). In contrast, the lower SLP off the North American coast enhances the southwesterly wind stress in the western Atlantic basin by about 30% in CCSM* (not shown). We note that during the winter months, there are larger magnitude SLP differences between CCSM* and CCSM poleward of 30° in both hemispheres. These differences are particularly large in the North Pacific and North Atlantic storm track regions (exceeding −2 mbar) and north of Siberia (exceeding +4 mbar).

[47] In the coupled cases, the subtropical and subpolar gyre circulations are about 10 Sv larger than in the uncoupled experiments presented in Figure 8. However, the BSF difference distributions for CCSM*-CCSM have very similar patterns to those of OCN*-OCN as shown in Figure 8b. Nevertheless, there are some differences in magnitudes, i.e., the positive difference regions along the NAC and south of Iceland are generally larger by more than 5 Sv and the negative difference region is slightly weaker by a few Sv in the vicinity of 35°W, 50°N in the CCSM*-CCSM differences than in the OCN*-OCN differences. Therefore, we conclude that the changes in the oceanic barotropic circulation are primarily due to the effects of the OFP on the deep ocean currents and that the wind stress changes play a secondary role.

[48] We finally show the time mean Northern Hemisphere sea ice concentrations from CCSM* and CCSM along with their differences in Figure 18. The largest differences, indicating a loss of sea ice, occur in the Nordic Sea and are due to the warmer SSTs in that region with the OFP. The resulting sea ice distribution compares more favorably with the observations as indicated by the 10% observational contour line. In particular, much too extensive sea ice just east of Iceland is reduced in CCSM*. The sea ice in the Arctic Ocean is mostly thinner in CCSM* than in CCSM by 4–20 cm, partly due to warmer surface air temperatures in CCSM* (not shown).

6. Summary and Discussions

[49] A new overflow parameterization of density-driven flows through ocean ridges via narrow, unresolved channels has been developed and successfully implemented in the CCSM4 ocean component. This parameterization represents

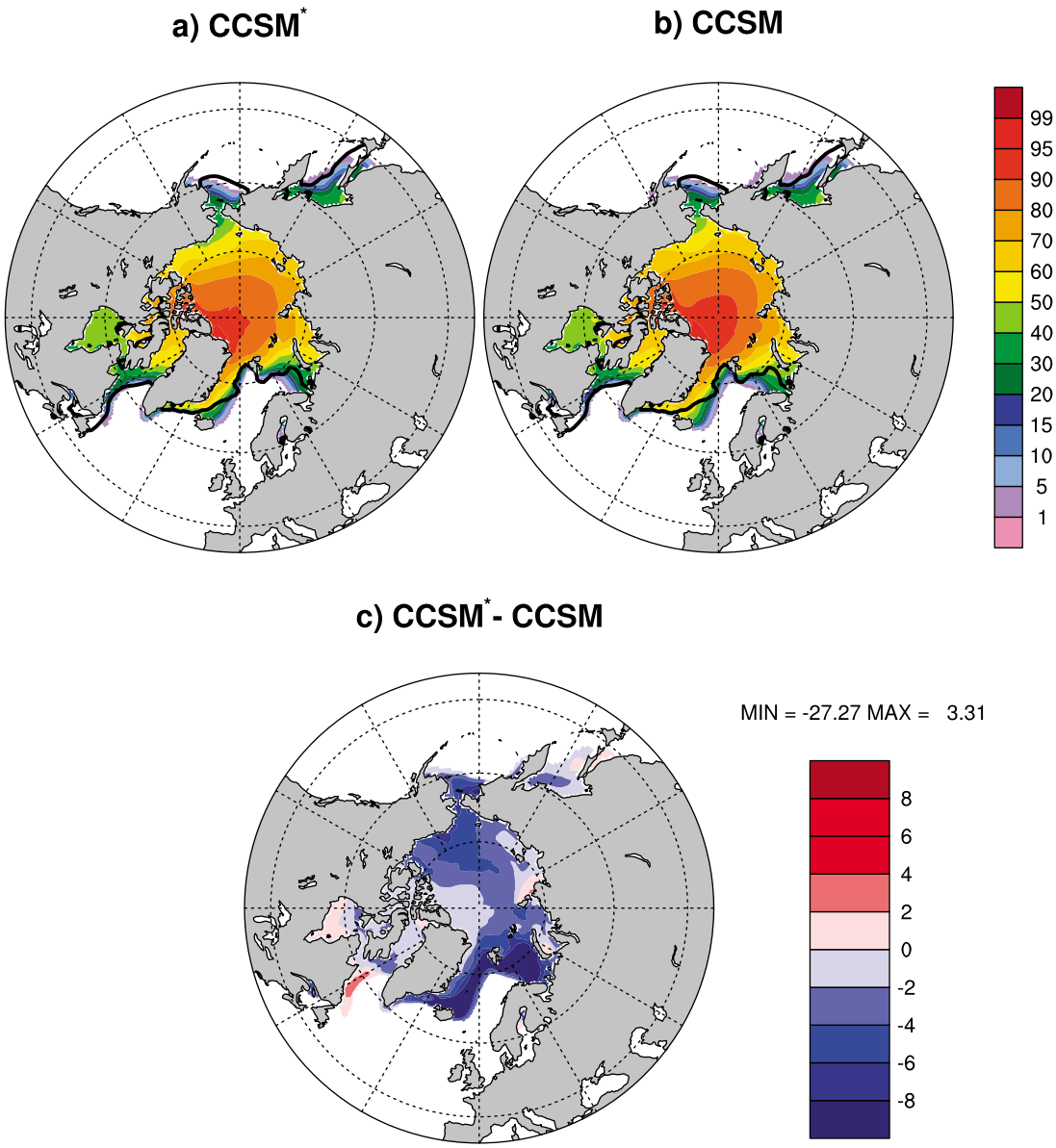

Figure 18. Time mean Northern Hemisphere sea ice concentration (% of grid area) from (a) CCSM* and (b) CCSM. (c) The CCSM*-CCSM difference distribution is given. In Figures 18a and 18b, the 10% concentration contours taken from Special Sensor Microwave Imager data [*Cavalieri et al.*, 1996] are also shown as thick black lines.

exchanges through narrow straits and channels, associated entrainment, and subsequent injection of overflow product waters into the abyssal basins. These overflow physics have been largely absent in today's OGCMs used in climate studies, because their explicit representation is prohibitively expensive, requiring fine resolutions both in the horizontal and vertical. Furthermore, the flows over staircase topography in a level coordinate model tend to have excessive convective entrainment, resulting in deep waters that are too light and that remain too shallow. Thus, even if a model with a cold Nordic Sea produces the densest possible source waters, the product water properties and injection depth will be quite different than observed due to poorly represented mixing. The present overflow parameterization (OFP) is based on the Marginal Sea Boundary Condition (MSBC) scheme of *Price and Yang* [1998]. However, there are significant differences between the two. These include calculations of the overflow properties that are based on the evolving model state and a new treatment of the baroclinic and barotropic momentum and continuity equations.

[50] We have investigated the impacts of the parameterized Denmark Strait (DS) and Faroe Bank Channel (FBC) overflows on the ocean circulation and climate, particularly focusing on the Atlantic Meridional Overturning Circulation (AMOC) and the North Atlantic climate. We consider two uncoupled and two fully coupled simulations. Each set consists of one case with the OFP and a control integration without it. The uncoupled and coupled simulations produce stable overflow properties. In both, the DS and FBC source volume transports are within the range of observed esti-

mates. The entrainment volume transports remain lower than observed, leading to similarly lower product volume transports in comparison with observational estimates. Due to low entrainment, the product water properties largely reflect those of the source waters. The overflow temperature and salinity properties are in better agreement with observations in the uncoupled case than in the coupled simulation, reflecting surface flux differences in the latter. For the DS, the product water injection depth of 1969 m in both uncoupled and coupled simulations is in very good agreement with observational estimates. The FBC injection depth of 2187 m in both cases is lower than in observations.

[51] The most significant impact of the OFP is the substantial reduction of the chronic shallow D_{AMOC} problem associated with the NADW penetration depth in level coordinate models. For example, D_{AMOC} = 4650 m in uncoupled OFP case is in excellent agreement with the 4200 ≤ D_{AMOC} ≤ 4500 m range from the RAPID data. In contrast, D_{AMOC} remains at 2900 m without the OFP. This improvement is due to the deeper penetration of the southward flowing Deep Western Boundary Current (DWBC) with the OFP and elimination of poleward flow. Associated with these improvements, the abyssal ventilation rates and the northward heat transport increase in the North Atlantic. The latter improves comparisons with observations, particularly in the uncoupled simulation. In the uncoupled case with the OFP, the warm bias of the control simulation in the deep North Atlantic has been substantially reduced. There are noticeable reductions also in the salinity biases in the northern North Atlantic in this case. Similar, but more modest bias reductions occur in the deep temperature and salinity distributions especially in the northern North Atlantic in the coupled OFP case compared to its control simulation.

[52] The coupled simulations show the climate impacts of the OFP through changes in the SSTs. In particular, the SSTs are warmer by >5°C off the North American coast and by >1°C in the Nordic Sea with the OFP. The surface heat flux changes mostly act to reduce these SST changes and exceed 140 W m^{-2} off the North American coast. There are related changes in the sea level pressure, leading to about 15% weaker westerly wind stress in the northern North Atlantic. In response to the warmer Nordic Sea SSTs, there are reductions in the sea ice extent, improving comparisons with observations. The top of the atmospheric model heat flux imbalance is 0.38 W m^{-2} in the control coupled simulation. It is reduced to 0.24 W m^{-2} with the OFP. Nevertheless, the Arctic surface air temperatures are warmer in the OFP case, contributing to slightly thinner sea ice in the Arctic Ocean compared to the control case.

[53] The subtropical and subpolar gyre circulation differences between the overflow and control cases are very similar in the uncoupled and coupled simulations. The Gulf Stream and North Atlantic Current paths are displaced northward with the OFP. As a consequence, the Northern Recirculation Gyre, already rather weak in the control cases, is absent in the overflow cases. Because this behavior is present in both uncoupled and coupled experiments, we believe that it is primarily due to the deep ocean circulation changes resulting from the parameterized overflows. Given the complex relationships between the Gulf Stream, North Atlantic Current, DWBC, and Labrador Sea basin properties, such degradations of some aspects of the barotropic circulation, despite significant improvements in the deep North Atlantic and Labrador Sea circulations, is not surprising.

[54] The major discrepancy with observations is the low entrainment rates even when the observed ocean state is used in the OFP equations. Modifications of some of the input parameters can certainly boost the entrainment volume transports, making them comparable to observations. Unfortunately, prognostic model simulations with such changed parameters eventually produced much shallower product water depths due to lighter product water densities in our experience. In this work, we remained faithful to the end-point entrainment model and did not explore the impacts of larger or multiple entrainment regions on the entrainment rates. Furthermore, recent studies by *Lauderdale et al.* [2008] and *Cenedese and Adduce* [2010] indicate entrainment occurring over long distances, i.e., between the Denmark Strait and Cape Farewell, at subcritical Froude numbers can increase the entrained volume transport. This is in addition to the entrainment occurring near the sill. It is also unclear how some recent parameterizations [e.g., *Jackson et al.*, 2008; *Ilicak et al.*, 2008a, 2008b; *Cenedese and Adduce*, 2010] would perform in comparison with the OFP in global OGCM simulations in which the parameterizations interact with continuously evolving ocean states. Exploration of these factors as well as comparisons with other parameterizations, however, are beyond the scope of the present study.

[55] Along with the Labrador Sea deep convection, the DS and FBC overflow waters supply the NADW, directly affecting the AMOC. At present, there is intense interest in the AMOC and its variability, largely due to potential predictability of its variations on decadal time scales. This is based on coupled modeling studies, showing prominent decadal variability in their AMOCs. However, a proper representation of the Nordic Sea overflows is either completely absent or rather ad hoc in these models. Therefore, how these overflows impact the AMOC variability is an open question. Indeed, our preliminary simulations with CCSM4 indicate muted AMOC variability with the OFP due to its stabilizing effects.

Appendix A: Summary of the OFP

[56] In this appendix, we present a general summary of the OFP and refer to *Briegleb et al.* [2010] for further details of the equations and their derivations as well as our particular model implementation and model time stepping. In addition, we only define new variables and refer to section 2 and Table 1 for the definitions of the others. The OFP consists of two parts: (1) calculation of the overflow properties based on the evolving ocean model state, and (2) OGCM modifications of the model boundary conditions, equations, and bottom topography.

A1. Calculation of the Overflow Properties

[57] The overflows are driven by the density difference at the sill depth between a Nordic Sea source, ρ_s, and the

Atlantic Ocean interior density, ρ_i, as expressed by the source reduced gravity

$$g'_s = \frac{\rho_s - \rho_i}{\rho_0} g. \tag{A1}$$

An equation of state is then used to compute ρ_i and ρ_s at the sill depth:

$$\rho_i = \rho(T_i, S_i, d_s), \quad \rho_s = \rho(T_s, S_s, d_s). \tag{A2}$$

Here, T and S represent volume-average potential temperature and salinity, respectively, over the horizontal regions shown in Figure 2. at the level containing the sill depth grid.

[58] As long as $g'_s > 0$ source overflow transport will occur. Assuming that W_s is greater than the radius of deformation and the return flow is not geometrically constrained, following *Whitehead et al.* [1974], M_s is obtained using the expression for rotating, hydraulically controlled maximum geostrophic flow through a strait

$$M_s = \frac{g'_s h_u^2}{2f} = \frac{9}{8} \frac{g'_s h_s^2}{f}, \tag{A3}$$

In (A3), h_u is the upstream source thickness, and following *Whitehead et al.* [1974], h_s is calculated from h_u as

$$h_s = \frac{2}{3} h_u. \tag{A4}$$

Assuming a rectangular cross sectional area with height h_s and width W_s at the strait exit, an associated source speed, U_s, can be evaluated

$$U_s = \frac{M_s}{h_s W_s}. \tag{A5}$$

As the source water accelerates down the continental slope, it spreads in width and thins. Near the shelf-slope break, it entrains ambient waters of the Atlantic Ocean. These processes are parameterized using the end-point model of an entraining, rotating density current developed by *Price and Baringer* [1994]. The entrainment is driven by the entrainment reduced gravity given by

$$g'_e = \frac{\rho'_s - \rho_e}{\rho_0} g, \tag{A6}$$

where

$$\rho'_s = \rho(T_s, S_s, d_e), \quad \rho_e = \rho(T_e, S_e, d_e), \tag{A7}$$

with ρ'_s and ρ_e are the source and entrainment region densities, respectively, both computed at d_e, using volume-average T and S for the corresponding lateral regions shown in Figure 2. As long as $M_s > 0$ and $g'_e > 0$ entrainment can occur.

[59] At the shelf break, the flow is assumed to have a characteristic speed governed by geostrophic balance

$$U_{geo} = \frac{g'_e \alpha}{f}. \tag{A8}$$

The average flow speed between the channel exit and the shelf break point is then given by

$$U_{avg} = 0.5\left(U_s + U_{geo}\right). \tag{A9}$$

The spreading is assumed to increase linearly with distance from the sill such that when the source water reaches the shelf break it has width W_{ssb} given by

$$W_{ssb} = W_s + 2K_{geo} x_{ssb} \tag{A10}$$

with the Ekman number, K_{geo}, specified by the ratio of bottom drag to Coriolis force over downslope flow

$$K_{geo} = \frac{C_d U_{avg}}{0.5 f \left(h_s + h_{geo}\right)}. \tag{A11}$$

At the shelf break, the thickness is given by

$$h_{geo} = \frac{U_s h_s W_s}{U_{geo} W_{ssb}}. \tag{A12}$$

Our particular definition of K_{geo} in (A11) follows the discussion given by *Wu et al.* [2007] and is based on U_{avg} and the average of thicknesses at the sill and at the shelf break, i.e., $0.5(h_s + h_{geo})$. Equations (A10–A12) can be solved simultaneously for h_{geo}.

[60] A geostrophic Froude number, F_{geo}, for the entrainment mixing at the shelf-break is defined as

$$F_{geo} = U_{geo} / \sqrt{g'_e h_{geo}} \tag{A13}$$

from which an entrainment parameter, ϑ, representing the ratio of entrained to product water volume transports, can be evaluated as

$$\vartheta = \frac{M_e}{M_p} = 1 - F_{geo}^{-2/3}. \tag{A14}$$

For $g'_e \le 0$ or $F_{geo} \le 1$, $M_e = 0$. Given M_s, M_e can be calculated using

$$M_e = M_s \frac{\vartheta}{1 - \vartheta} = M_s \left(F_{geo}^{2/3} - 1\right). \tag{A15}$$

Using volume conservation, the product volume transport is then

$$M_p = M_s + M_e. \tag{A16}$$

Finally, from tracer conservation, the product water potential temperature and salinity are calculated using

$$T_p = T_s(1 - \vartheta) + T_e \vartheta, \quad S_p = S_s(1 - \vartheta) + S_e \vartheta. \tag{A17}$$

A2. OGCM Modifications

[61] In POP [see *Smith et al.*, 2010], the model variables are discretized on the Arakawa B grid [*Arakawa and Lamb*, 1977] in the horizontal in which the tracers and horizontal velocity components are located at the cell centers and corners, respectively. In the following, we refer to these as T grid and U grid. As in many other ocean models [c.f.,

Griffies et al., 2004], POP also employs a baroclinic-barotropic split method to solve the momentum equations. With this split, the total velocity is written as

$$u = u' + U \tag{A18}$$

where u' and U are the baroclinic and barotropic velocities, respectively. They are defined by

$$U = \frac{1}{H+\eta}\int_{-H}^{\eta} u dz, \qquad \frac{1}{H+\eta}\int_{-H}^{\eta} u' dz = 0. \tag{A19}$$

In (A19), z is the vertical coordinate, positive upward, η is the free surface displacement relative to $z = 0$, and H is the depth at the U grid points.

[62] We assume that the side wall overflow velocities represent the total velocity u. For those U grid columns where these overflow velocities occur, H must be extended downward to the bottom of the vertical grid level where the overflow velocities are actually specified to be consistent with the definitions in (A19). This must be done for source, entrainment, and product columns. The new depth is given by

$$H' = H + \Sigma \Delta z \tag{A20}$$

where Δz denotes the vertical level thicknesses and the summation is done for the side wall heights from H down to the bottom of the overflow level. To avoid complications arising from moving product water injection locations, we change H to H' at all N_p product water sites. If the overflow level is several vertical grid levels below H, the thicknesses of the levels in between are included in this summation. These in-between levels are assumed to have $u = 0$. Thus, we replace H with H' in all model equations where appropriate, including any relevant vertical integrals. For example, (A19) becomes

$$U = \frac{1}{H'+\eta}\int_{-H'}^{\eta} u dz, \qquad \frac{1}{H'+\eta}\int_{-H'}^{\eta} u' dz = 0. \tag{A21}$$

As described by *Smith et al.* [2010], POP first solves the momentum equations, without including the surface pressure gradient, for an auxiliary velocity u'^*, giving us u'^* between $-H \le z \le \eta$. The relationship between this intermediate velocity and u' is

$$u' = u'^* - \frac{1}{H'+\eta}\int_{-H'}^{\eta} u'^* \, dz = u'^* - \overline{u'^*}. \tag{A22}$$

Our assumption of $u = 0$ at the side walls between H and any overflow velocity levels leads to $u' = -U$ at these in-between levels. Similarly, because $u = u_{OVF}$, we have $u' = u_{OVF} - U$ at all the overflow velocity locations. Here, $u = u_{OVF}$ is a generic variable used to indicate the overflow velocities. So, knowing U (see below), u'^* between $-H \le z \le \eta$, and u' between $-H' \le z < -H$, we use (A21) and (A22) to obtain an equation for $\overline{u'^*}$ for the entire column

$$\overline{u'^*} = \frac{1}{H}\left[\int_{-H}^{\eta} u'^* \, dz + \int_{-H'}^{-H} u' \, dz\right]. \tag{A23}$$

We then evaluate u' using (A22) for $-H \le z \le \eta$. This process results in local volume conservation, consistent with the imposed overflow velocities, for the T grid columns to the immediate upstream (to the right in Figure 1) of the source and to the immediate downstream (to the left in Figure 1) of the entrainment and product locations.

[63] These velocity modifications obviously impact the horizontal velocity divergences, thus destroying the local volume conservation, at the T grid columns immediately downstream (to the left in Figure 1) of the source and immediately upstream (to the right in Figure 1) of the entrainment and product injection sites. For example, the T grid column above the raised sill has a nonzero vertical velocity at the bottom of the column. The magnitudes of these imbalances are equal to the volume transports associated with the source, entrainment, and product waters for each affected column. Therefore, we modify the vertically integrated continuity equation for these columns to account for these transports and thus enforce continuity, viz.,

$$\frac{\partial \eta}{\partial t} + \nabla \cdot (H' + \eta)U - q_w - \delta_{OVF}\frac{M_{OVF}}{\Delta A} = 0 \tag{A24}$$

where t is time, q_w is the freshwater flux, δ_{OVF} is 1 for the affected columns and 0 elsewhere, M_{OVF} represents either M_s, M_e, or M_p, and ΔA is the appropriate surface area of the affected T grid columns. (A24) together with the vertically integrated momentum equation are then used to compute both η and U. It is important to reiterate here that the last term on the left hand side of (A24) accounts for the changes in the horizontal velocity divergences within a specified T grid column and it should not be viewed as mass (volume) injections/extractions from either the surface or the ocean bottom.

[64] The changes in the tracer equations are relatively straightforward compared to the momentum equations. Specifically, the advection algorithms are modified to incorporate the nonhomogeneous flux boundary conditions at the overflow sites. By construction, this process conserves all tracers.

Appendix B: Summary of Observed DS and FBC Overflow Properties

[65] Some observational estimates of the DS and FBC overflow properties are given in Tables 2 and 3, respectively. We mostly rely on the Table of Observations (TO) presented in *Legg et al.* [2009] for T, S, and ρ. This TO represents a collection of existing observations of gravity currents. For volume transports, we report estimates from various sources to particularly stress observational uncertainty and temporal and spatial variabilities as shown by some recent observational studies. Such variability undoubtedly exists in T and S as well, but only a few of the observational values are also included in Tables 2 and 3. The transport estimates from different sources can be based on different methods and different density criterion, thus further contributing to the differences between the estimates. For example, $M_s = 2.1 \pm 0.2$ Sv given in Table 3 for the FBC from *Dye et al.* [2007] is based on the observed velocity field from the bottom to the level at which the velocity has one half of its maximum value [see also *Hansen and Osterhus*, 2007]. When they use only the volume flux of

water denser than 1027.8 kg m^{-3}, the estimate becomes M_s = 1.9 ± 0.3 Sv. We note that observational studies usually provide only the source and product water properties as the entrainment properties are very difficult to measure. We calculate the M_e estimates given in Tables 2 and 3 as the implied transports based on the differences between observational estimates of M_p and M_s.

[66] Recent studies by *Macrander et al.* [2005] and *Macrander et al.* [2007] find that the DS M_s varies between 2.6 and 3.8 Sv, suggesting significant interannual variability in contrast with some previous studies [e.g., *Dickson and Brown*, 1994]. *Macrander et al.* [2005] also report a large T_s range of $-0.4 \leq T_s \leq 0.7$°C. We note that our OFP calculations indicate that this range in T_s can account for a range of M_s variability from 2.8 to 3.4 Sv, assuming nothing else changes. Some evidence for spatial and temporal variability of the entrainment and subsequent product water transports can be found in Figure 11 of *Girton and Sanford* [2003]. Starting with a mean M_s = 2.7 Sv, their downstream sliding mean estimates show M_p = 3.9 Sv at about 180 km downstream of the sill. This implies an entrainment transport of only 1.2 Sv. Both of these M_e and M_p estimates are lower than the TO and *Dickson and Brown* [1994] M_e and M_p of 2.3 and 5.2 Sv, respectively.

[67] Using repeat section measurements in the FBC, *Mauritzen et al.* [2005] show that the source water transport varies considerably, i.e., $1.5 \leq M_s \leq 3.5$ Sv, with a mean M_s = 2.4 Sv. This range certainly includes the other M_s estimates listed in Table 3. The westernmost section located at 150 km downstream of the sill shows that the product water transport ranges between 2.5–2.9 Sv with a mean M_p = 2.7 Sv in *Mauritzen et al.* [2005]. This M_p implies a mean M_e of only 0.3 Sv. In contrast, the section located at 100 km downstream of the sill has $3.0 \leq M_p \leq 4.2$ Sv with a mean M_p = 3.6 Sv. These measurements clearly reveal the large variability in these transports, exposing the difficulties in capturing such variability in some observational studies, using short records only at a few locations. The ranges of $0 \leq T_p \leq 6$°C and $34.9 \leq S_p \leq 35.15$ psu given in *Mauritzen et al.* [2005] are broad enough to include the other respective estimates. We note, however, that a recent observational study by *Dye et al.* [2007] finds much smaller variability in their estimates of the FBC M_s in contrast with *Mauritzen et al.* [2005].

[68] **Acknowledgments.** We thank members of the Climate Process Team (CPT) on Gravity Current Entrainment (GCE) for helpful interactions. In particular, we thank Jim Price for providing his Marginal Sea Boundary Condition code and very useful discussions. We also thank Wanli Wu for his contributions during the early stages of this work. This study was supported by the NSF grants OCE-0336834 and OCE-0611486 for the CPT-GCE. The computational resources were provided by the Computational and Information Systems Laboratory of the National Center for Atmospheric Research (NCAR). NCAR is sponsored by the National Science Foundation. Data from the RAPID-WATCH MOC monitoring project are funded by the U.K. Natural Environment Research Council and are freely available from www.noc.soton.ac.uk/rapidmoc.

References

Arakawa, A., and V. R. Lamb (1977), The UCLA general circulation model, *Meth. Comput. Phys.*, *17*, 174–265.

Beckmann, A., and R. Doescher (1997), A method for improved representation of dense water spreading over topography in geopotential coordinate models, *J. Phys. Oceanogr.*, *27*, 581–591.

Born, A., A. Levermann, and J. Mignot (2009), Sensitivity of the Atlantic Ocean circulation to a hydraulic overflow parameterization in a coarse resolution model: Response of the subpolar gyre, *Ocean Modell.*, *27*, 130–142, doi:10.1016/j.ocemod.2008.11.006.

Briegleb, B. P., and B. Light (2007), A Delta-Eddington multiple scattering parameterization for solar radiation in the sea ice component of the Community Climate System Model, *Tech. Note NCAR/TN-472+STR*, 100 pp., Natl. Cent. for Atmos. Res., Boulder, Colo.

Briegleb, B. P., C. M. Bitz, E. C. Hunke, W. H. Lipscomb, M. M. Holland, J. L. Schramm, and R. E. Moritz (2004), Scientific description of the sea ice component in the Community Climate System Model, version three, *Tech. Note NCAR/TN-463+STR*, 70 pp., Natl. Cent. for Atmos. Res., Boulder, Colo.

Briegleb, B. P., G. Danabasoglu, and W. G. Large (2010), An overflow parameterization for the ocean component of the Community Climate System Model, *Tech. Note NCAR/TN-481+STR*, 72 pp., Natl. Cent. for Atmos. Res., Boulder, Colo.

Broecker, W. S. (2003), Does the trigger for abrupt climate change reside in the ocean or in the atmosphere?, *Science*, *300*, 1519–1522.

Bryan, F. O., G. Danabasoglu, N. Nakashiki, Y. Yoshida, D.-H. Kim, J. Tsutsui, and S. C. Doney (2006), Response of the North Atlantic thermohaline circulation and ventilation to increasing carbon dioxide in CCSM3, *J. Clim.*, *19*, 2382–2397.

Campin, J.-M., and H. Goosse (1999) Parameterization of density-driven downsloping flow for a coarse resolution ocean model in z coordinate, *Tellus Ser. A*, *51*, 412–430.

Cavalieri, D., C. Parkinson, P. Gloersen, and H. J. Zwally (1996), Sea Ice Concentrations From Nimbus-7 SMMR and DMSP SSM/I Passive Microwave Data, http://nsidc.org/data/nsidc-0051.html, Natl. Snow and Ice Data Cent., Boulder, Colo. (Updated 2008.)

Cenedese, C., and C. Adduce (2010), A new parameterization for entrainment in overflows, *J. Phys. Oceanogr.*, *40*, 1835–1850, doi:10.1175/2010JPO4374.1.

Chang, Y. S., Z. D. Garraffo, H. Peters, and T. M. Ozgokmen (2009), Pathways of Nordic overflows from climate model scale and eddy resolving simulations, *Ocean Modell.*, *29*, 66–84, doi:10.1016/j.ocemod.2009.03.003.

Comiso, J. (1999), Bootstrap Sea Ice Concentrations for NIMBUS-7 SMMR and DMSP SSM/I, http://nsidc.org/data/nsidc-0079.html, Natl. Snow and Ice Data Cent., Boulder, Colo. (Updated 2002.)

Cunningham, S. A., et al. (2007), Temporal variability of the Atlantic meridional overturning circulation at 26.5°N, *Science*, *317*, 935–938, doi:10.1126/science.1141304.

Danabasoglu, G. (2008), On the multidecadal variability of the Atlantic meridional overturning circulation in the Community Climate System Model version 3, *J. Clim.*, *21*, 5524–5544, doi:10.1175/2008JCLI2019.1.

Danabasoglu, G., and J. Marshall (2007), Effects of vertical variations of thickness diffusivity in an ocean general circulation model, *Ocean Modell.*, *18*, 122–141, doi:10.1016/j.ocemod.2007.03.006.

Danabasoglu, G., W. G. Large, J. J. Tribbia, P. R. Gent, B. P. Briegleb, and J. C. McWilliams (2006), Diurnal coupling in the tropical oceans of CCSM3, *J. Clim.*, *19*, 2347–2365.

Danabasoglu, G., R. Ferrari, and J. C. McWilliams (2008), Sensitivity of an ocean general circulation model to a parameterization of near-surface eddy fluxes, *J. Clim.*, *21*, 1192–1208, doi:10.1175/2007JCLI1508.1.

Delworth, T., S. Manabe, and R. J. Stouffer (1993), Interdecadal variations of the thermohaline circulation in a coupled ocean-atmosphere model, *J. Clim.*, *6*, 1993–2011.

Dickson, R. R., and J. Brown (1994), The production of North Atlantic Deep Water: Sources, rates, and pathways, *J. Geopyhs. Res.*, *99*, 12,319–12,341.

Doney, S. C., and M. W. Hecht (2002), Antarctic bottom water formation and deep-water chlorofluorocarbon distributions in a global ocean climate model, *J. Phys. Oceanogr.*, *32*, 1642–1666.

Dye, S., B. Hansen, S. Osterhus, D. Quadfasel, B. Rudels (2007), The overflow of dense water across the Greenland-Scotland Ridge, *CLIVAR Exchanges*, *12*, 20–22.

Emms, P. W. (1997), Streamtube models of gravity currents in the ocean, *Deep Sea Res. Part I*, *44*, 1575–1610.

Enmar, L., K. Borenas, I. Lake, and P. Lundberg (2009), Comments on "Is the Faroe Bank Channel overflow hydraulically controlled?" *J. Phys. Oceanogr.*, *39*, 1534–1538, doi:10.1175/2008JPO4020.1.

Ferrari, R., J. C. McWilliams, V. M. Canuto, and M. Dubovikov (2008), Parameterization of eddy fluxes near oceanic boundaries, *J. Clim.*, *21*, 2770–2789, doi:10.1175/2007JCLI1510.1.

Fischer, J., F. A. Schott, and M. Dengler (2004), Boundary circulation at the exit of the Labrador Sea, *J. Phys. Oceanogr.*, *34*, 1548–1570.

Fox-Kemper, B., R. Ferrari, and R. Hallberg (2008a), Parameterization of mixed layer eddies: Part I. Theory and diagnosis, *J. Phys. Oceanogr.*, *38*, 1145–1165, doi:10.1175/2007JPO3792.1.

Fox-Kemper, B., G. Danabasoglu, R. Ferrari, and R. W. Hallberg (2008b), Parameterizing submesoscale physics in global climate models, *CLIVAR Exchanges*, *13*, 3–5.

Gent, P. R., and J. C. McWilliams (1990), Isopycnal mixing in ocean circulation models, *J. Phys. Oceanogr.*, *20*, 150–155.

Gettelman, A., H. Morrison, and S. J. Ghan (2008), A new two-moment bulk stratiform cloud microphysics scheme in the Community Atmospheric Model (CAM3): Part II. Single-column and global results, *J. Clim.*, *21*, 3660–3679.

Ghan, S. J., and R. C. Easter (2006), Impact of cloud-borne aerosol representation on aerosol direct and indirect effects, *Atmos. Chem. Phys.*, *6*, 4163–4174.

Ghan, S. J., and R. A. Zaveri (2007), Parameterization of optical properties for hydrated internally mixed aerosol, *J. Geophys. Res.*, *112*, D10201, doi:10.1029/2006JD007927.

Girton, J. B., and T. B. Sanford (2003), Descent and modification of the overflow plume in the Denmark Strait, *J. Phys. Oceanogr.*, *33*, 1351–1363.

Girton, J. B., L. J. Pratt, D. A. Sutherland, and J. F. Price (2006), Is the Faroe Bank Channel overflow hydraulically controlled? *J. Phys. Oceanogr.*, *36*, 2340–2349.

Griffies, S. M., and K. Bryan (1997), Predictability of North Atlantic multidecadal climate variability, *Science*, *275*, 181–184.

Griffies, S. M., et al. (2000), Developments in ocean climate modelling, *Ocean Modell.*, *2*, 123–192.

Griffies, S. M., M. J. Harrison, R. C. Pacanowski, and A. Rosati (2004), A technical guide to MOM4, *GFDL Ocean Group Tech. Rep. 5*, NOAA Geophys. Fluid Dyn. Lab., Princeton, N. J. (Available online at http://www.gfdl.noaa.gov/fms.)

Griffies, S. M., et al. (2005), Formulation of an ocean model for global climate simulations, *Ocean Science*, *1*, 45–79.

Griffies, S. M., et al. (2009), Coordinated Ocean-ice Reference Experiments (COREs), *Ocean Modell.*, *26*, 1–46, doi:10.1016/j.ocemod.2008.08.007.

Hallberg, R. (2000), Time integration of diapycnal diffusion and Richardson number dependent mixing in isopycnal coordinate ocean models, *Mon. Weather Rev.*, *128*, 1402–1419.

Hansen, B., and S. Osterhus (2007), Faroe Bank Channel overflow 1995–2005, *Prog. Oceanogr.*, *75*, 817–856, doi:10.1016/j.pocean.2007.09.004.

Holland, M. M., C. M. Bitz, E. C. Hunke, W. H. Lipscomb, and J. L. Schramm (2006), Influence of the sea ice thickness distribution on polar climate in CCSM3, *J. Clim.*, *19*, 2398–2414.

Hunke, E. C., and W. H. Lipscomb (2008), CICE: The Los Alamos sea ice model documentation and software user's manual, version 4.0, *Tech. Rep. LA-CC-06-012*, Los Alamos Natl. Lab., Los Alamos, N. M.

Hurrell, J. W., et al. (2006), Atlantic climate variability and predictability: A CLIVAR perspective, *J. Clim.*, *19*, 5100–5121.

Hurrell, J. W., J. J. Hack, D. Shea, J. M. Caron, and J. Rosinski (2008), A new sea surface temperature and sea ice boundary data set for the Community Atmosphere Model, *J. Clim.*, *21*, 5145–5153, doi:10.1175/2008JCLI2292.1.

Iacono, M. J., J. S. Delamere, E. J. Mlawer, M. W. Shephard, S. A. Clough, and W. D. Collins (2008), Radiative forcing by long-lived greenhouse gases: Calculations with the AER radiative transfer models, *J. Geophys. Res.*, *113*, D13103, doi:10.1029/2008JD009944.

Ilicak, M., T. M. Ozgokmen, H. Peters, H. Z. Baumert, and M. Iskandarani (2008a), Very large eddy simulation of the Red Sea overflow, *Ocean Modell.*, *20*, 183–206, doi:10.1016/j.ocemod.2007.08.002.

Ilicak, M., T. M. Ozgokmen, H. Peters, H. Z. Baumert, and M. Iskandarani (2008b), Performance of two-equation turbulence closures in three-dimensional simulations of the Red Sea overflow, *Ocean Modell.*, *24*, 122–139, doi:10.1016/j.ocemod.2008.06.001.

Ilicak, M., T. M. Ozgokmen, E. Ozsoy, and P. F. Fischer (2009), Nonhydrostatic modeling of exchange flows across complex geometries, *Ocean Modell.*, *29*, 159–175, doi:10.1016/j.ocemod.2009.04.002.

Jackson, L., R. Hallberg, and S. Legg (2008), A parameterization of shear-driven turbulence for ocean climate models, *J. Phys. Oceanogr.*, *38*, 1033–1053, doi:10.1175/2007JPO3779.1.

Jayne, S. R. (2009), The impact of abyssal mixing parameterizations in an ocean general circulation model, *J. Phys. Oceanogr.*, *39*, 1756–1775.

Jochum, M. (2009), Impact of latitudinal variations in vertical diffusivity on climate simulations, *J. Geophys. Res.*, *114*, C01010, doi:10.1029/2008JC005030.

Jochum, M., G. Danabasoglu, M. Holland, Y.-O. Kwon, and W. G. Large (2008), Ocean viscosity and climate, *J. Geophys. Res.*, *113*, C06017, doi:10.1029/2007JC004515.

Joyce, T. M., J. Dunworth-Baker, R. S. Pickart, D. Torres, and S. Waterman (2005), On the Deep Western Boundary Current south of Cape Cod, *Deep Sea Res. Part II*, *52*, 615–625.

Killworth, P. D. (1977), Mixing on the Weddell Sea continental slope, *Deep Sea Res.*, *24*, 427–448.

Killworth, P. D., and N. R. Edwards (1999), A turbulent bottom boundary layer code for use in numerical ocean models, *J. Phys. Oceanogr.*, *29*, 1221–1238.

Kosters, F. (2004), Denmark Strait overflow: Comparing model results and hydraulic transport estimates, *J. Geophys. Res.*, *109*, C10011, doi:10.1029/2004JC002297.

Kosters, F., R. H. Kase, A. Schmittner, and P. Herrmann (2005), The effect of Denmark Strait overflow on the Atlantic meridional overturning circulation, *Geophys. Res. Lett.*, *32*, L04602, doi:10.1029/2004GL022112.

Large, W. G., and G. Danabasoglu (2006): Attribution and impacts of upper-ocean biases in CCSM3, *J. Clim.*, *19*, 2325–2346.

Large, W. G., and S. Yeager (2004), Diurnal to decadal global forcing for ocean and sea-ice models: The data sets and flux climatologies, *Tech. Note NCAR/TN-460+STR*, 105 pp., Natl. Cent. for Atmos. Res., Boulder, Colo.

Large, W. G., and S. G. Yeager (2008), The global climatology of an interannually varying air-sea flux data set, *Clim. Dyn.*, *33*, 341–364, doi:10.1007/s00382-008-0441-3.

Large, W. G., J. C. McWilliams, and S. C. Doney (1994), Oceanic vertical mixing: A review and a model with a nonlocal boundary layer parameterization, *Rev. Geophys.*, *32*, 363–403.

Large, W. G, G. Danabasoglu, S. C. Doney, J. C. McWilliams (1997), Sensitivity to surface forcing and boundary layer mixing in a global ocean model: Annual mean climatology, *J. Phys. Oceanogr.*, *27*, 2418–2447.

Lauderdale, J. M., S. Bacon, A. C. N. Garabato, and N. P. Holliday (2008), Intensified turbulent mixing in the boundary current system of southern Greenland, *Geophys. Res. Lett.*, *35*, L04611, doi:10.1029/2007GL032785.

Legg, S., et al. (2009), Improving oceanic overflow representation in climate models: The Gravity Current Entrainment Climate Process Team, *Bull. Am. Meteorol. Soc.*, *90*, 657–670, doi:10.1175/2008BAMS2667.1.

Levitus, S., T. Boyer, M. Concright, D. Johnson, T. O'Brien, J. Antonov, C. Stephens, and R. Garfield (1998), *World Ocean Database 1998*, vol. 1, *Introduction*, *NOAA Atlas NESDIS*, vol. 18, 346 pp., NOAA, Silver Spring, Md.

Lipscomb, W. H., E. C. Hunke, W. Maslowski, and J. Jakacki (2007), Ridging, strength, and stability in high-resolution sea ice models, *J. Geophys. Res.*, *112*, C03S91, doi:10.1029/2005JC003355.

Macrander, A., U. Send, H. Valdimarsson, S. Jonsson, and R. H. Kase (2005), Interannual changes in the overflow from the Nordic Seas into the Atlantic Ocean through Denmark Strait, *Geophys. Res. Lett.*, *32*, L06606, doi:10.1029/2004GL021463.

Macrander, A., R. H. Kase, U. Send, H. Valdimarsson, and S. Jonsson (2007), Spatial and temporal structure of the Denmark Strait overflow revealed by acoustic observations, *Ocean Dyn.*, *57*, 75–89.

Mauritzen, C., J. Price, T. Sanford, and D. Torres (2005), Circulation and mixing in the Faroese Channels, *Deep Sea Res. Part I*, *52*, 883–913.

Meehl, G. A., et al. (2006), Climate change projections for the twenty-first century and climate change commitment in the CCSM3, *J. Clim.*, *19*, 2597–2616.

Mlawer, E. J., S. J. Taubman, P. D. Brown, M. J. Iacono, and S. A. Clough (1997), Radiative transfer for inhomogeneous atmospheres: RRTM, a validated correlated-k model for the longwave, *J. Geophys. Res.*, *102*, 16,663–16,682.

Morrison, H., and A. Gettelman (2008), A new two-moment bulk stratiform cloud microphysics scheme in the Community Atmospheric Model (CAM3): Part I. Formulation and numerical tests, *J. Clim.*, *21*, 3642–3659.

Nakashiki, N., D.-H. Kim, F. O. Bryan, Y. Yoshida, D. Tsumune, K. Maruyama, and H. Kitabata (2006), Recovery of thermohaline circulation under CO_2 stabilization and overshoot scenarios, *Ocean Modell.*, *15*, 200–217, doi:10.1016/j.ocemod.2006.08.007.

Neale, R. B., J. H. Richter, and M. Jochum (2008), The impacts of convection on ENSO: From a delayed oscillator to a series of events, *J. Clim.*, *21*, 5904–5924, doi:10.1175/2008JCLI2244.1.

Oleson, K., et al. (2010), Technical description of the Community Land Model version 4, *Tech. Note NCAR/TN-478+STR*, 266 pp., Natl. Cent. for Atmos. Res., Boulder, Colo.

Price, J., and M. O. Baringer (1994), Outflows and deep water production by marginal seas, *Prog. Oceanogr.*, *33*, 161–200.

Price, J., and J. Yang (1998), Marginal sea overflows for climate simulations, in *Ocean Modeling and Parameterization*, edited by E. P. Chassignet and J. Verron, pp. 155–170, Kluwer Acad., Dordrecht, Netherlands.

Riemenschneider, U., and S. Legg (2007), Regional simulations of the Faroe Bank Channel overflow in a level model, *Ocean Modell.*, *17*, 93–122, doi:10.1016/j.ocemod.2007.01.003.

Roberts, M. J., and R. A. Wood (1997), Topographic sensitivity studies with a Bryan-Cox-Type ocean model, *J. Phys. Oceanogr.*, *27*, 823–836.

Roberts, M. J., R. Marsh, A. L. New, and R. A. Wood (1996), An intercomparison of a Bryan-Cox-Type ocean model and an isopycnic ocean model: Part I. The subpolar gyre and high-latitude processes, *J. Phys. Oceanogr.*, *26*, 1495–1527.

Smith, P. C. (1975), A streamtube model for the bottom boundary currents in the ocean, *Deep Sea Res. Oceanogr. Abstr.*, *22*, 853–874.

Smith, R. D., et al. (2010), The Parallel Ocean Program (POP) reference manual, Ocean component of the Community Climate System Model (CCSM), *Tech. Rep. LAUR-10-01853*, 141 pp., Los Alamos Natl. Lab., Los Alamos, N. M. (Available online at http://www.ccsm.ucar.edu/models/ccsm3.0/pop.)

Spall, M. A. (1996), Dynamics of the Gulf Stream/Deep Western Boundary Current crossover: Part I. Entrainment and recirculation, *J. Phys. Oceanogr.*, *26*, 2152–2168.

St. Laurent, L. C., H. L. Simmons, and S. R. Jayne (2002), Estimates of tidally driven enhanced mixing in the deep ocean, *Geophys. Res. Lett.*, *29*(23), 2106, doi:10.1029/2002GL015633.

Steele, M., R. Morley, and W. Ermold (2001), PHC: A global ocean hydrography with a high quality Arctic Ocean, *J. Clim.*, *14*, 2079–2087.

Tang, Y. M., and M. J. Roberts (2005), The impact of a bottom boundary layer scheme on the North Atlantic Ocean in a global coupled climate model, *J. Phys. Oceanogr.*, *35*, 202–217.

Thiele, G., and J. L. Sarmiento (1990), Tracer dating and ocean ventilation, *J. Geophys. Res.*, *95*, 9377–9391.

Whitehead, J. A., A. Leetmaa, and R. A. Knox (1974), Rotating hydraulics of strait and sill flows, *Geophys. Fluid Dyn.*, *6*, 101–125.

Winton, M., R. Hallberg, and A. Gnanadesikan (1998), Simulation of density-driven frictional downslope flow in z-coordinate ocean models, *J. Phys. Oceanogr.*, *28*, 2163–2174.

Wu, W., G. Danabasoglu, and W. G. Large (2007), On the effects of parameterized Mediterranean overflow on North Atlantic Ocean circulation and climate, *Ocean Modell.*, *19*, 31–52, doi:10.1016/j.ocemod.2007.06.003.

Xu, X., Y. S. Chang, H. Peters, T. M. Ozgokmen, and E. P. Chassignet (2006), Parameterization of gravity current entrainment for ocean circulation models using a high-order 3D nonhydrostatic spectral element model, *Ocean Modell.*, *14*, 19–44, doi:10.1016/j.ocemod.2006.02.006.

Yeager, S. G., and M. Jochum (2009), The connection between Labrador Sea buoyancy loss, deep western boundary current strength, and Gulf Stream path in an ocean circulation model, *Ocean Modell.*, *30*, 207–224, doi:10.1016/j.ocemod.2009.06.014.

B. P. Briegleb, G. Danabasoglu, and W. G. Large, National Center for Atmospheric Research, PO Box 3000, Boulder, CO 80307, USA. (bruceb@ucar.edu; gokhan@ucar.edu; wily@ucar.edu)